THERMAL HYDRAULIC PERFORMANCE OF ALUMINUM METAL FOAM

HEAT EXCHANGERS WITH VARYING CELLULAR LATTICE STRUCTURES

A Thesis

by

EDWARD AUGUST KRAFT IV

Submitted to the Office of Graduate and Professional Studies of
Texas A&M University
in partial fulfillment of the requirements for the degree of

MASTER OF SCIENCE

Chair of Committee,	Mark Kimber
Committee Members,	Karen Kirkland
	Alaa Elwany
Head of Department,	Yassin Hassan

August 2018

Major Subject: Nuclear Engineering

ABSTRACT

Due to their large surface area to volume ration, low density, and high strength

structure, aluminum metal foams offer a promising application for heat exchangers. One

significant design challenge of aluminum foam heat exchangers is optimizing the trade-

off between heat transfer performance and pressure drop (i.e., pumping power). Previous

experimental investigations successfully quantified the thermal hydraulic behavior of

such heat exchangers based on foam porosity, but they provide limited insight on the

effects of varying cellular lattice structures within their samples. As a result, a

Computational Fluid Dynamic (CFD) analysis using Star CCM+ is carried out for the

thermal hydraulic behavior of aluminum foam heat exchangers based on varying cellular

lattice structures. Two secondary studies were also undertaken, including the comparison

of the thermal-hydraulic performance using different meshing styles (structured vs

unstructured) and different CFD software (Star CCM+ vs ANSYS Fluent).

Pressure drop and heat transfer performance were analyzed based on three

criteria: unit cell geometry, relative density, and orientation. Performance rankings were

developed according to pressure drop and heat transfer. Pressure drop and Nusselt

number correlations were formed for heat sink designs. It is recommended to use models

with unstructured mesh for pressure drop data and models with structured mesh for

thermal data. Finally, both CFD codes resulted in nearly identical pressure drop and

thermal data.

ACKNOWLEDGEMENTS

CONTRIBUTORS AND FUNDING SOURCES

Contributors

This work was supervised by a thesis committee consisting of Professor Mark Kimber of the Department of Nuclear Engineering and Professors Karen Kirkland of the Department of Nuclear Engineering and Alaa Elwany of the Department of Mechanical Engineering.

The experimental data analyzed for Chapter 3 Section 3.1 was provided by Kevin Laux under the direction of Dr. Albert To of the Department of Mechanical Engineering & Materials Science at the University of Pittsburgh.

All other work conducted for the thesis was completed by the student independently.

TABLE OF CONTENTS

LIST OF FIGURES

LIST OF TABLES

CHAPTER 1

INTRODUCTION

1.1 Porous Media

Porous media have been a topic of great importance for many decades, and even longer. In fact, establishing flow models and pressure drop relations dates back to the 19th century [1] for studying the underground water table. This, along with the numerous studies that followed, have established porous media as a fully independent branch of fluid mechanics. Porous media in heat transfer applications also has a rich history beginning with the wicking process in heat pipes [2] enabled through what at that time were new fabrication methods (e.g., sintering or small feature extrusion processes). In a generalized sense, the heat exchanger applications make use of a metal foam, which can be engineered to be lightweight with high strength and a high heat transfer area per unit volume [3]. These metal foams and new fabrication methods have enabled engineers to consider an increasingly wide range of additional applications.

Due to their large surface-area-to-volume ratio and enhanced flow mixing, metal foams offer a promising application for heat exchangers. Heat exchangers are widely known and used to transfer heat between one flow loop and another. There are several thermal management issues that need more efficient heat exchangers for heat removal. For example, the increasing demand for higher performance in modern computers has led to high heat fluxes at the chip level [4]. The challenge is to use an effective cooling technique to remove as much heat as possible without overheating the system. Metal

foam heat exchangers are considered as one potential solution for thermal management applications, where a large amount of heat can be transferred over a small volume.

Depending of their production process, metal foams can be classified as either "open-cell" or "closed-cell". Open-celled metal foams are often used in applications such as compact heat exchangers [5], heat sinks for power electronics [6], and coal combustors [7]. More applications are expected in the future, particularly because low density foams with uniform and regular cell structures are currently being developed with affordable manufacturing processes. Closed-cell metal foams have been developed since the 1950s, but commercial production didn't begin until the 1990s. This class of metal foams are primarily used as an impact-absorbing material.

Most metal foam investigations have focused on analyzing open-celled metal foams because of their high porosity ($\varepsilon > 0.90$). Calmidi and Mahajan [8] addressed heat conduction in open-celled aluminum metal foams. By taking into the account ligament diameter, pores per inch, pore size, and porosity, they gathered experimental data to develop an analytical model for the thermal conductivity. Lee et al. [9] considered metal foams as high performance air-cooled heat sinks for electronics packages. Experimentally, he found that aluminum foams could dissipate heat fluxes up to 100 W/cm^2 while maintaining a junction temperature below 95°C. Hsieh et al. [10] performed an experiment to characterize the thermal-hydraulic behavior of several aluminum foam heat sinks with different porosities (0.87-0.96).

Open cell metal foams are manufactured in a powder metallurgical replication technique. The method allows the processing of almost all materials which are available

2

in powder form. The matrix of cells and ligaments is completely repeatable, regular, and uniform throughout the entirety of the material. Most manufacturing companies produce these foams based on density (3-12%) and pores per inch (5, 10, 20, 40).

Although this manufacturing method is capable of creating uniform cell structures, there are a few design limitations. It is difficult to maintain constant ligament diameter throughout the cell structure. Previous open-cell metal foam investigations have measured the average ligament diameter for their analytical models, thus causing some error in their results. Another huge limitation is the inability to create specific cell geometries that can be patterned throughout the complete structure. The shape of these cells are sphere-like and comprised of 8-10 pores.

Most of the previous analytical and experimental studies examine the thermal-hydraulic performance of these open-cell metal foams using an unstructured network of cells. Their results are analytically expressed by varying several parameters: porosities, pores per inch, ligament diameter, and pore size. One limitation of these and other studies stems from the fact that this common fabrication method does not allow uniform ligament size throughout the foam, and this prevents one from gaining valuable insight into the role that cell geometry plays in the overall thermal and flow performance. An alternative fabrication technique is additive manufacturing, where the engineer has much tighter control over the geometric features of the metal foam. This approach has begun to gain interest, but represents previously unexplored regions of operating conditions. One of the primary goals of this thesis is to provide a framework for predicting heat sink performance in these regions.

1.2 Additive Manufacturing

Additive Manufacturing (AM) is an appropriate name to describe the technologies that build 3D objects by adding layer-upon-layer of material. Some of the practical materials manufactured include plastic, metal, and concrete. Common to AM technologies is the use of a computer, 3D modeling software (CAD), 3D printer, and a layering material. After a CAD sketch is created, the AM system reads the data from the CAD file and adds subsequent layers of liquid, powder, or sheet material in a layer-upon-layer pattern to fabricate a 3D object.

AM technologies have been studied and developed commercially since the late 1980s. Some of these processes include Fused Deposition Modeling (FDM) [13], Stereolithography [14], Selective Laser Sintering (SLS) [15], and Three Dimensional Printing (3DP) [16]. These technologies provide distinct advantages for choosing AM over other manufacturing processes. The first is free complexity, which is one of the most favorable AM abilities. It actually costs less to print a complex part instead of a simple cube of the same size. The more complex, or the less solid the object is, the faster and cheaper it can be made. Another advantage is free variety. The capacity for free variety with few constraints allows parts to be printed fast by changing the original CAD file. Anything that can be designed in CAD software can be creating with AM. The AM process is also fast with little lead time. Engineers can create a prototype with a 3-D printer immediately after creating a part's STL file. This allows the engineers to test the part immediately instead of waiting weeks or months for a prototype or part to arrive.

These advantages make additive manufacturing a promising method to designing efficient heat sinks and heat exchangers.

1.3 Lattice Optimization

To design an efficient heat exchanger or heat sink, a low pressure drop is needed between the fluid inlet and outlet to achieve a pumping system with moderate power requirements. A high heat transfer coefficient and large surface area are also needed in order for the heat to transfer rapidly through the medium. Therefore, one significant design challenge of aluminum foam heat exchangers is optimizing the trade-off between heat transfer performance and pressure drop (i.e., pumping power). These heat transfer and fluid friction losses are in direct competition with one another. The performance can be optimized by adjusting one against the other. These adjustments can be made by properly selecting physical properties such as unit cell geometry and relative density for optimal parameters.

Cheng et al. [17] worked with cellular structures to design an optimization methodology that redesigns additive manufactured components with reduced material while still maintaining the structural integrity. They determined that the most important characteristic of a cellular solid is its relative density. By knowing the mechanical properties of a component and its density distribution, the proposed optimization method reconstructs the component by replacing the low density sections with cellular lattices. For example, the strength of an additive manufactured beam was increased by 75% and stiffness by more than 110% by implementing the proposed optimization method.

While significant advances have been made in regard to structural optimization, little has been done to analyze the thermal properties of these structured foams. Understanding the thermal properties of the cellular lattices could eventually allow the lattice to be optimized with both the thermal and mechanical loads in mind. Previous work has focused on obtaining the mechanical properties of various lattice structures with their respective correlations.

While the long term vision is optimizing the lattice structure for both mechanical and thermal properties for additive manufactured geometries, the focus of this thesis is establishing pressure drop and heat transfer correlations along with findings that will reduce computation time. This is done by means of Computation Fluid Dynamics (CFD). Chapter Two of this thesis will focus on an experimental setup, where collected data is used for comparison to the CFD results for pressure drop. The numerical setup will be detailed in this section as well. Chapter Three will show the experimental and numerical pressure drop results, and Chapter Four will present the numerical heat transfer results. Finally, Chapter Five summarized the work with the project conclusions and discussion for future work.

CHAPTER 2

PROBLEM DESCRIPTION

2.1 Experimental Procedures

2.1.1 Manufactured Samples

The lattices were modeled in SolidWorks, which is a Computer Aided Design (CAD) package capable of modeling complex geometries. The resulting CAD files were imported to an EOS M 290 machine using an AlSi10Mg alloy to manufacture the samples. The EOS M 290 machine was selected due to its fast, flexible, and cost-effective production of metal components directly from CAD data. AlSi10Mg offers good strength, hardness, and dynamic properties. It is typically used for parts with thin walls and complex geometry. Seven samples were manufactured and composed of 8 x 8 x 8 unit cell cubes with the exception of one. Each unit cell occupies an area of 0.15 in^2 producing a total sample length of 1.2 in (30.48 mm). The samples have 0.025 in (0.64 mm) side and top walls in addition to a 0.1 in (2.54 mm) thick base surrounding the lattice. **Error! Reference source not found.** shows a manufactured sample. The base was designed to allow high flux regions from imperfect contact to dissipate slightly before the heat energy reached the lattice.

Figure 1. Frontal view of manufactured 8 x 8 x 8 lattice.

A total of seven samples were manufactured in order to analyze the thermal-fluid performance based on three criteria: unit cell geometry, unit cell orientation, and relative density (Table 1). Four of these samples were manufactured with a different unit cell geometry at a relative density of 40%. These geometries included a cubic, octet, midpoint, and diagonal structure, which can be seen in Figure 2. An additional cubic lattice was manufactured at 40% relative density, but with the unit cell rotated 45 degrees. To compare the thermal-hydraulic performance based on relative density, three samples were manufactured using the cubic unit cell with 20%, 40%, and 60% relative densities. Henceforth, the nomenclature used to identify a sample will be referenced by the unit cell geometry followed by relative density. For example, the sample comprised of cubic unit cells at a relative density of 40% will be referred to as Cubic40. The exception is the cubic unit cell rotated 45 degrees, which will be references as Cubic45deg.

Table 1. Properties of the additive manufactured samples.

Geometry	Cubic	Cubic	Cubic	Cubic	Octet	Midpoint	Diagonal
Relative Density (%)	20	40	40	60	40	40	40
Orientation (degrees)	0	0	45	0	0	0	0

| Cubic | Octet | Midpoint | Diagonal |
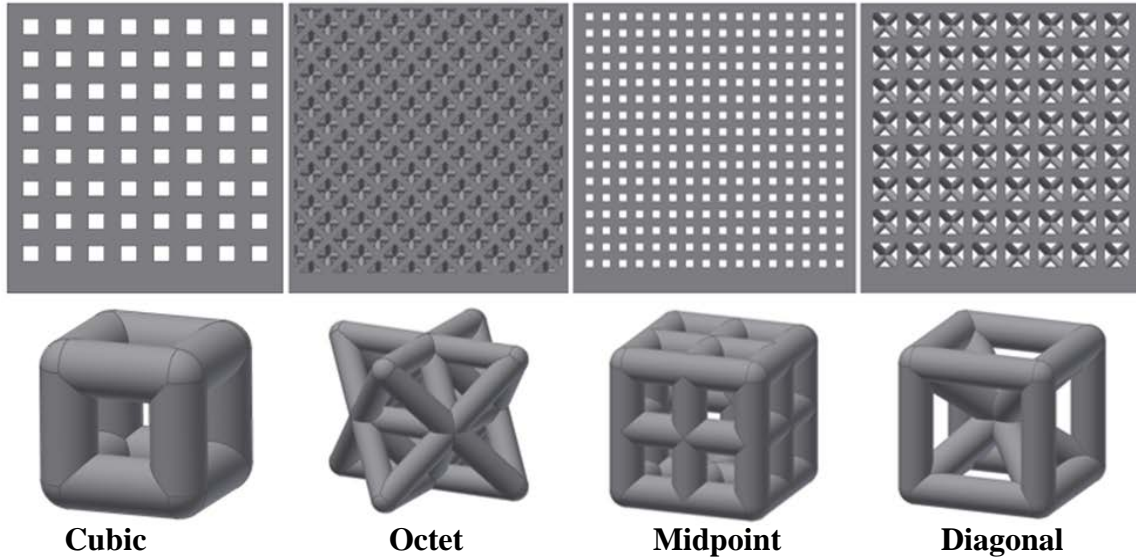
Figure 2. Sample inlets with their respective unit cell geometry.

2.1.2 Experimental Setup

The experimental setup was built and the samples were tested by a colleague at

the University of Pittsburgh. Enough details are included here in order to provide the

proper backdrop for comparisons between this data and the numerical simulations later

on. The setup consisted of a small wind tunnel to provide flow through the samples. The

working fluid was air and was supplied from the building at room temperature. Although

the building supply was set at 90 psig, this was reduced to 65 psig to ensure that small

fluctuations in building supply did not affect air flow rate through the experiment.

Figure 3 shows the schematic of the experiment, and Table 2 lists the equipment used. The mass flow rate was manually adjusted via a valve on the flow meter. An entrance channel with a length of 32.5 in (0.825 mm) allowed the flow to develop before reaching the test section. The cross section of the entrance length was 1.3 x 1.35 in, resulting in 24.5 hydraulic diameters. Air was delivered at ambient, so the assumption was made that the entrance length was adiabatic. Table 3 shows the experimental flow and heat properties.
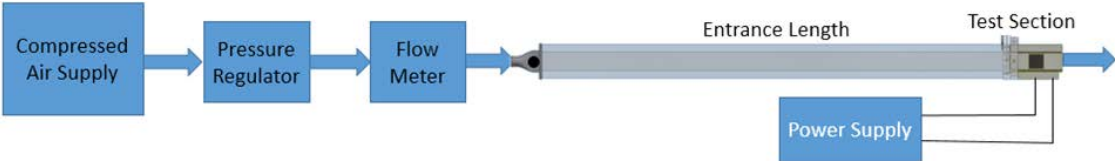
Figure 3. Experimental setup consisting of a several main components: compressed air supply, pressure regulator, flow meter, entrance length, test section, and power supply.

Table 2. Experimental equipment.

Device	Vendor	Model Number
Rotameter	Omega	FL50254-A
Manometer	Omega	HHC280
DAQ	Nation Instruments	9213
Anemometer Signal Conditioning	Dantec Dynamics	54T30
Anemometer DAQ	National Instruments	9215

Table 3. Experimental fluid and solid properties (air properties at 20°C).

Property	Value
ρ_{air} – Air Density	$1.2009\,\frac{kg}{m^3}$
μ_{air} – Dynamic Viscocity	$1.8335 \times 10^{-5}\,Pa \cdot s$
k_{air} – Air Thermal Conductivity	$0.0260\,\frac{W}{m \cdot K}$
Cp_{air} – Air Specific Heat	$1007\,\frac{J}{kg \cdot K}$
ρ_{solid} – Solid Density	$2702\,\frac{kg}{m^3}$
k_{solid} – Solid Thermal Conductivity	$110\,\frac{W}{m \cdot K}$
T_{inlet} – Inlet Temperature	$300\,K$
Q – Heat Power Input	$60.4\,W$

A differential pressure measurement was performed across the sample by placing two pressure ports just before the inlet and right after the outlet of the sample. Figure 4 shows a side view of the test section. The pressure measurements depend solely on the axial distance between ports (length of the sample plus 0.30 in) and did not vary from left to right. Therefore, pressure was measured on the flow's centerline.
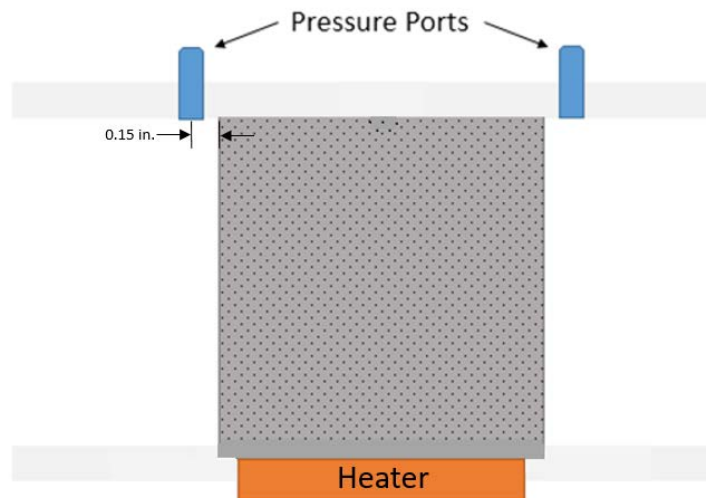
Figure 4. Test section side view.

Pressure drop measurements were made at volumetric flow rates from 2-14 SCFM or until the sensor limit of 10 kPa was exceeded. Measurements were made along this range in 1 SCFM increments. Each sample was tested twice by taking ascending and descending measures. After each flow rate adjustment, the pressure was allowed to equalize for 30 seconds before a measurement was recorded. The volumetric flow rate was converted to the average entrance channel velocity by first converting SCFM to CFM. This was calculated by using Eq. (2.1). By knowing the entrance channel cross sectional area, the average velocity in this section was easily found.

$$[CFM] = [SCFM]\frac{P_{atm}}{\Delta P + P_{atm}} \tag{2.1}$$

Velocity profiles were measured before the test section in the vertical and diagonal direction from the centerline of the flow. A hot-wire anemometer was placed at the entrance channel centerline and a measurement was recorded. Additional measurements were taken every 0.0625 in for each direction up until the wall. The profiles were measured at flow rates of 2, 5, 8, and 10 SCFM. By using the hot-wire anemometer calibration curve (Figure 5), the anemometer voltage output was converted to a velocity. By using this conversion, velocity profiles were measured at each of the four flow rates. Figure 6 and Figure 7 show the normalized velocity profiles in the vertical and diagonal direction, respectively. An exponential curve fit was applied to each profile resulting in an R-squared value greater than 0.98. The curve fitted velocity profiles will be discussed in more detail in the numerical setup section.
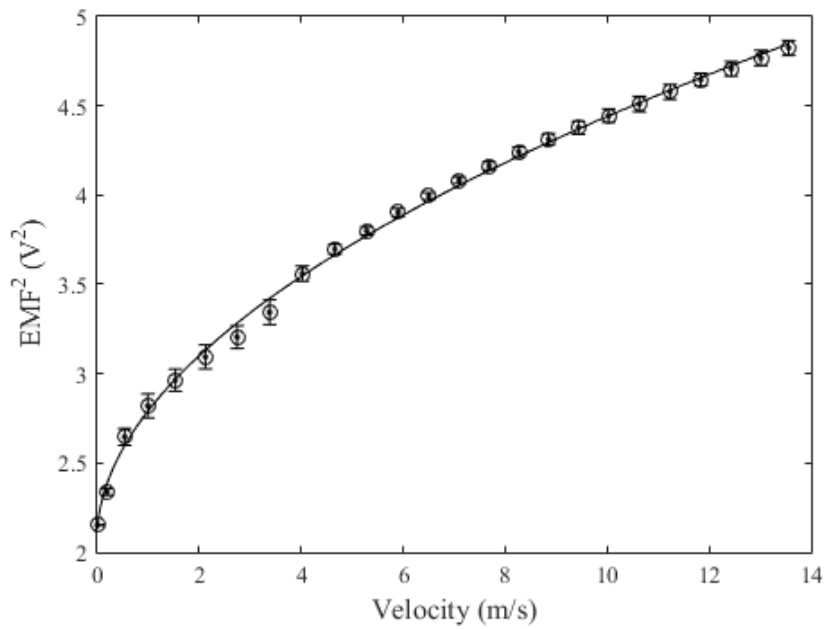
Figure 5. Hot-wire anemometer calibration curve.
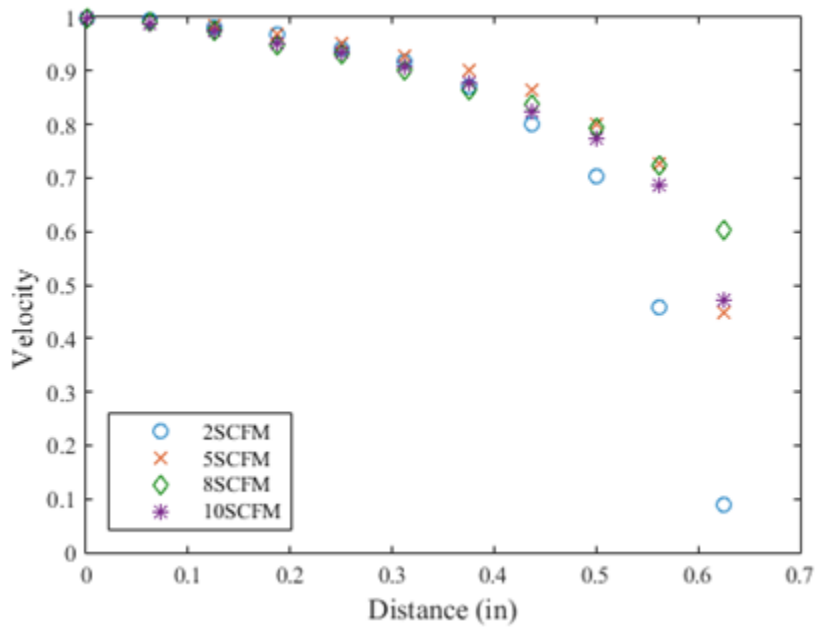
Figure 6. Normalized velocity profiles in the vertical direction from centerline to wall. Profiles are normalized by their respective centerline values.
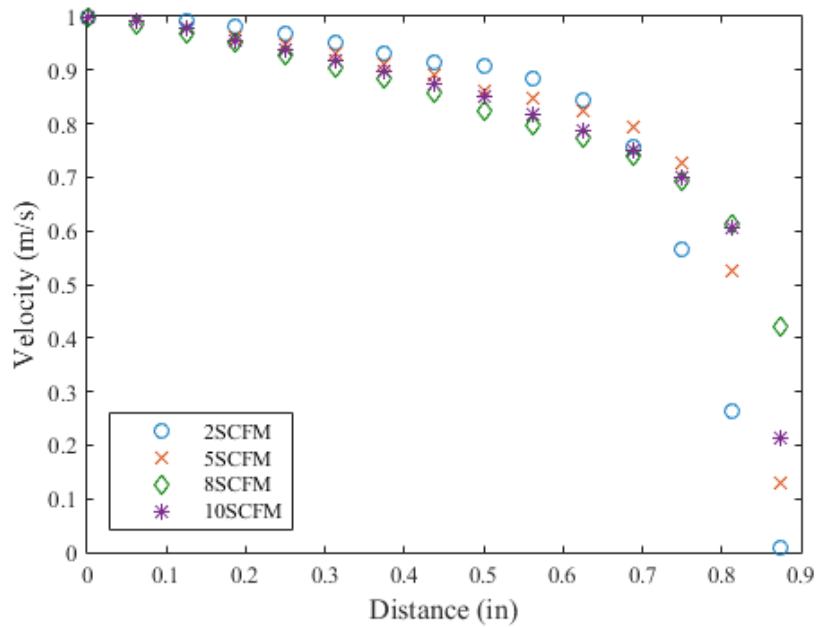
Figure 7. Normalized velocity profiles in the diagonal direction from centerline to wall.

2.2 Computation Procedures

2.2.1 Pressure Drop

Computational fluid dynamics (CFD) enables one to solve the strongly coupled

non-linear partial differential equations describing the flow physics in terms of velocity,

pressure, and temperature. The application of CFD has quickly expanded over the past

few decades resulting today in many commercially available codes well capable of

solving the current flow characteristics. Star CCM+ 11.06 was the chosen CFD software

to compare to the experimental data as it offers an efficient and accurate set of fluid

dynamics models and solvers. It also provides excellent parallel performance and

scalability.

The first step in modeling the pressure drop across the samples numerically was to extract the fluid in the solid CAD models. Only the fluid needed to be modeled to determine pressure drop. Once extracted, an inlet and outlet channel were attached to the fluid. The inlet channel had the same dimensions as the entrance channel used in the experimental setup. The outlet channel was 1.5 in, so the outlet pressure could be modified to avoid flow reversal. The fluid CAD models were saved as a Parasolid file. Parasolid is a geometric modeling kernel that has the capabilities of retaining a 3D model's geometry, and other important details.

Since the flow simulations (and especially the later heat transfer simulations) could become computationally expensive, some exploratory tests were conducted to determine whether useful information could be ascertained from a subset of the complete geometry. A quick test was carried out by comparing the pressure drop across a full scale model (8 x 8 x 8) compared to a quarter symmetric model (4 x 4 x 8). The initial conditions and flow properties were the same for both cases. The resulting pressure drops differed by 0.06%. Therefore, quarter-symmetry was applied for each fluid CAD models before importing to the CFD software. Figure 8 shows the quarter-symmetric fluid CAD model for the Diagonal40 sample.
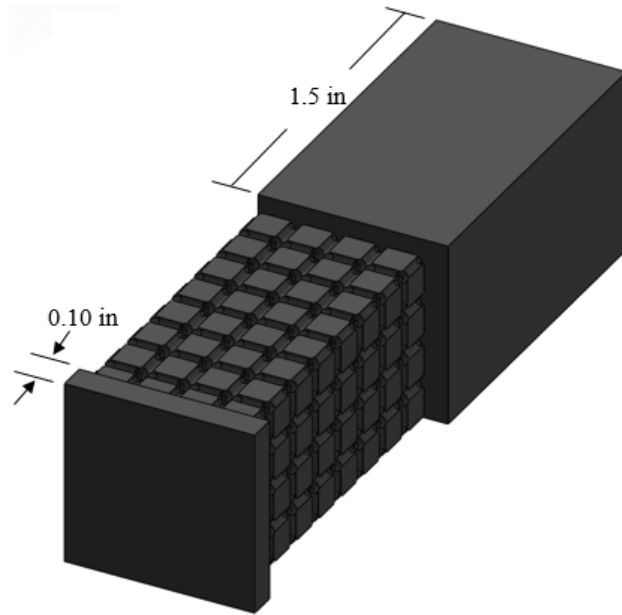
Figure 8. Quarter symmetric fluid CAD model of the Diagonal40 sample.

2.2.1.1 Unstructured Meshing

The fluid CAD models were imported to Star CCM+ and the domains were discretized with an unstructured mesh. The choice to use a structured or an unstructured mesh depends on the specific problem. Generating an unstructured mesh for complex geometry is usually much faster than structured mesh generation. Structured mesh generation with the octet and diagonal unit cells may take a substantial amount of time, as opposed to a few hours with an unstructured mesh generation. The fluid models were meshed with polyhedral cells. Polyhedral meshes provide a balanced solution for complex mesh generation problems. They are fast to converge, easy to generate, and more efficient than tetrahedral cells. A polyhedral mesh contains approximately five times fewer cells than a tetrahedral mesh [18].

Star CCM+ has several meshing models to help improve mesh quality. The Surface Remesher model improves the overall quality of an existing surface and optimizes it for the volume mesh models by retriangulating the surface. The Surface Wrapper model can be used to provide a closed, manifold, non-intersecting surface. It is mostly used for poor quality CAD data, but can also be used for overly complex geometry. This feature removes internal features, simplifies the surface geometry by removing unwanted detail, and closes holes and gaps. The Surface Remesher and Surface Wrapper were implemented in the mesh generation.

Prism layers were added next to the wall surfaces to improve the accuracy of the flow solution. A total of ten prism layers were added near the walls. The near wall prism layer thickness was set at 1×10^{-6} m. This thickness resulted in a $y^+ < 1$ at all walls, which is capable of solving the flow characteristics in the viscous sublayer region. The y^+ value is a non-dimensional distance for a wall-bounded flow. It is found by solving Eq. (2.1),

$$y^+ = \frac{yu_\tau}{\nu} \tag{2.1}$$

Where y is the normal distance from the wall to the wall-cell centroid, u_τ is the shear velocity, and ν is the kinematic viscosity of the fluid. The importance of having a $y^+ < 1$ at all walls will be further discussed when wall treatment is selected.

Three meshes were created for each sample: coarse, medium, and fine. By generating three meshes of different element counts, a Grid Convergence Index (GCI) method can be used to quantify the numerical uncertainty. All results will be from models discretized with a fine mesh. Table 4 shows the three mesh sizes for each model.

It is important to note that the Cubic45deg meshes are nearly double those from the other samples because quarter-symmetric conditions could not be applied. The Cubic45deg sample was not a true 8 x 8 x 8 unit cell lattice, therefore, half-symmetry conditions had to be applied. If quarter symmetry was applied, it would have resulted in a completely different manufactured sample. An example of a polyhedral unstructured fine mesh for the Midpoint40 model is displayed in Figure 9.

Table 4. Coarse, medium, and fine fluid mesh count for quarter-symmetric models.

	Number of Mesh Elements		
Sample	Coarse (million)	Medium (million)	Fine (million)
Cubic20	3.94	5.14	7.08
Cubic40	3.82	5.04	7.01
Cubic45deg	7.12	10.33	14.27
Cubic60	2.66	3.92	6.80
Diagonal40	3.94	5.35	8.46
Midpoint40	3.45	4.87	7.31
Octet40	3.76	5.24	7.71
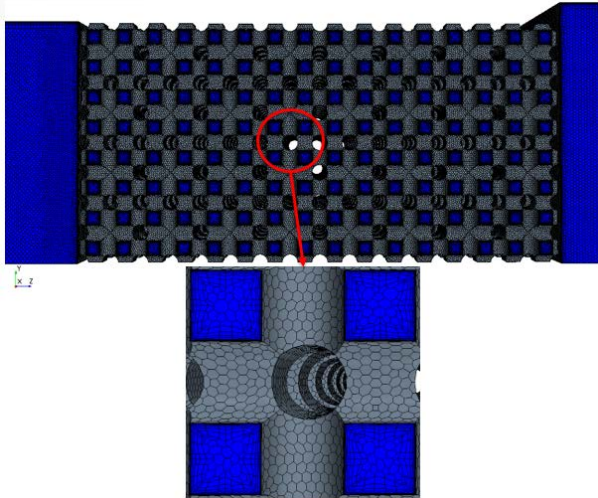
Figure 9. Polyhedral fine mesh for the Midpoint40 model.

A single unit cell from the Cubic20, Cubic40, and Cubic60 samples were also modeled. Unstructured meshes were generated using the same process as the quarter-symmetric models. The purpose of modeling a single unit cell is to quickly compare the solutions of an unstructured mesh model to a structured mesh model. The unstructured mesh element counts will be listed in the next section with the structured mesh element counts.

2.2.1.2 Structured Meshing

Generating a structured mesh over an unstructured mesh has significant advantages. Unstructured mesh requires large amounts of computational memory for storing nodes, elements, and a connectivity table to link them. On the other hand, a structured mesh is defined using a specific pattern which avoids the need to store any connectivity table. The structured mesh also has a high degree of control over precise cell numbers and refinement, thus making the discretization error calculation more accurate. An unstructured mesh generates interior modes automatically causing a desired total cell count to be challenging. Finally, a model with a structured mesh leads to more accurate results and better convergence. It is typically easier to capture the boundary layer with structured meshing.

A single fluid unit cell was modeled with structured mesh to compare the solutions to the model with unstructured mesh. Due to the complexity (and subsequent difficulty of generating a structured mesh) of the other unit cells, only the Cubic20, Cubic40, and Cubic60 fluid unit cells were modeled in this particular instance. The three

fluid unit cells were meshed using ANSYS ICEM CFD. This software has many basic

tools and methods for generating structured meshes. These methods allow the user the

freedom to generate a mesh as desired. ICEM CFD also provides mesh checking to fix

errors and clean the mesh to improve quality.

The CAD model of the cubic unit cell was imported into the meshing software as

a Parasolid file. After defining the surfaces, the cubic unit cell was blocked to provide a

projection-based mesh generation environment. The blocking feature allows the edges of

each individual block to have a specific node count. Figure 10 shows the blocking

strategy for the cubic unit cell with node specification. Prism layers were added and had

the same parameters as the unstructured mesh.
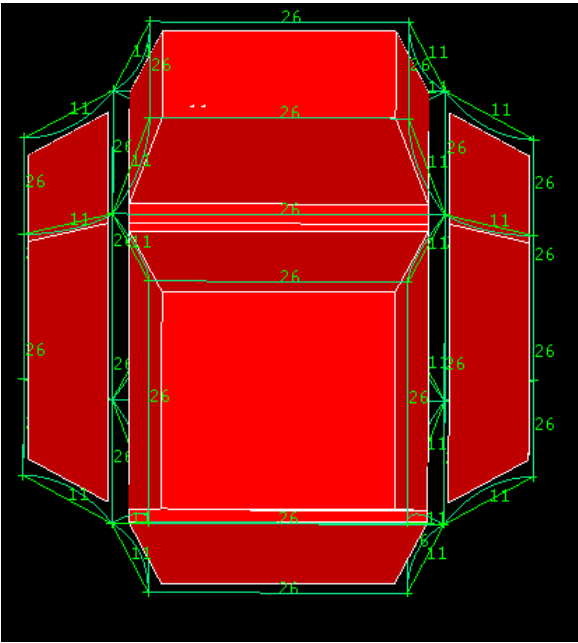
Figure 10. Blocking strategy used in ANSYS ICEM CFD with node specifications for all edges.

After blocking, node specification, and adding prism layers, the pre-mesh was computed to generate an initial mesh. The volume mesh was generated, and the resulting mesh contained hexahedral cells. The Check Mesh feature was used to find and fix possible errors such as duplicate elements, penetrating elements, multiple edges, and unconnected vertices. The mesh quality for all models were improved until the minimum cell quality was greater than 0.7.

A hexahedral mesh is generally more accurate than a tetrahedral mesh while having a lower cell count. The better accuracy is owed to maintaining orthogonal grids in the wall-normal direction for wall-bounded flows. The angles between faces for each element can be kept close to 90 degrees. Star CCM+ does not have a standard hexahedral meshing model as a tool, which is the reason for the unstructured meshes to consist of polyhedral cells. Although Star CCM+ and ANSYS ICEM CFD can produce tetrahedral meshes, the most accurate mesh type was selected: hexahedral for structured mesh and polyhedral for unstructured mesh. Table 5 shows the element count for the unstructured and structured single cubic unit cell models. The unstructured element counts were within 5% of the respective structured element counts. Figure 11 shows the mesh type comparison of the fine mesh for the Cubic20 unit cell.

Table 5. Element counts for the unstructured and structured single unit cell fluid meshes

Sample	Unstructured Element Count			Structured Element Count		
	Coarse	Medium	Fine	Coarse	Medium	Fine
Cubic20	36400	74700	145300	38000	76000	150000
Cubic40	37200	78300	152900	38000	76000	150000
Cubic60	39100	77000	148600	38000	76000	150000
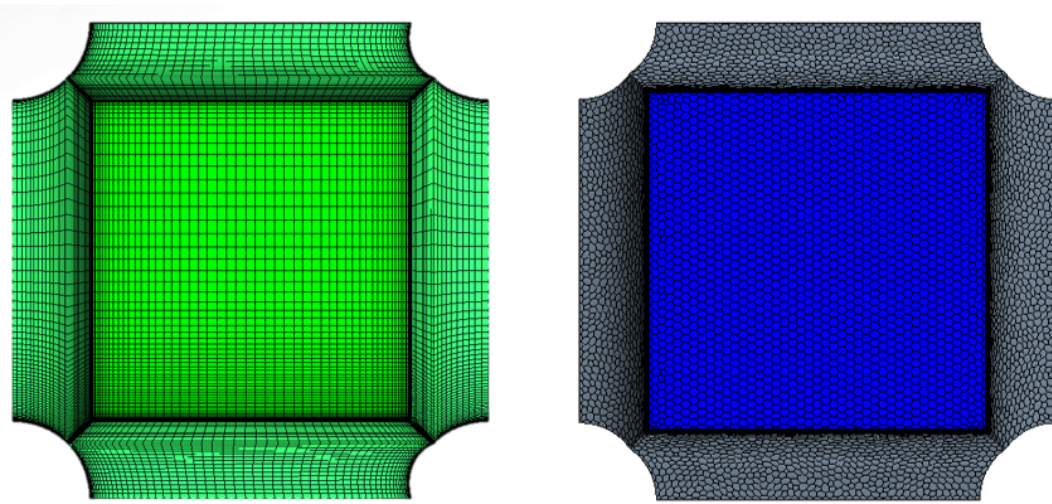
Figure 11. Fine structured mesh (left) vs fine unstructured mesh (right) of the Cubic20 fluid unit cell.

2.2.1.3 Simulation Setup

After generating meshes for each model, a turbulence model was selected to calculate the mean flow. It is known that turbulence models are not an exact representation of the physical phenomena, but based on different assumptions about the flow. Since there is not a single turbulence model suited for every type of flow problem, several turbulence models have been derived that reflect the current state of the art. A Della Torre [19] investigated the pressure drop in open-cell metal foams. They used Reynolds Averaged Navier-Stokes (RANS) CFD simulations to capture the pressure drop based on geometrical parameters.

A simple turbulence model study was conducted to decide which turbulence model could accurately capture the flow physics within the flow domain. Two models were selected based on the RANS equations: the k-ε and k-ω models. Both models are two equation models that solve two additional partial differential transport equations to

give a general description of turbulence. Five variations of the k-ε turbulence model were tested. The Standard k-ε model is a standard version of the two-equation model that solves for the turbulent kinetic energy and dissipation rate. The Realizable k-ε model contains a modified transport equation for the turbulence dissipation rate. This model provides results at least as accurate as the Standard k-ε model. The Realizable Two-Layer k-ε uses an approach that divides the computation into two layers. This allows the k-ε model to be applied in the viscous sublayer. The Eliptic Blending (EB) k-ε model implements the concept of elliptic relaxation to improve the existing Realizable k-ε model in the near-wall region. The Abe-Kondoh-Nagano (AKN) k-ε model has different coefficients and damping functions than the Standard k-ε model. It is known to work well with complex flows. The variations of the k-ε model tested were the Standard k-ω and k-ω SST models, which solves transport equations for the turbulent kinetic energy and specific dissipation rate.

To reduce computational time, the turbulence models were tested on a single unit cell instead of the full scale model. The Cubic40 and Octet40 were selected in order to accommodate the simplest (Cubic) and most complex (Octet) flow paths. All cases were simulated with the same boundary conditions and fluid properties with inlet velocities of 1 and 5 m/s. The cases were simulated for 2000 iterations to allow the solution to converge. All turbulence models resulted in pressure drops within 0.05% of each other for both velocity cases except for the Realizable k-ε Two-Layer model, which resulted in a pressure drop increase of 18.5% from all other cases. Therefore, a visual representation of the results will not be included. A turbulence model capable of solving the turbulence

23

effects accurately near the wall was desired. The additional pressure drop solved by the

Realizable k-ε Two-Layer model was most likely contributed from the viscous sublayer.

The Realizable k-ε Two-Layer model was selected as it is a fast, two-equation model

capable of solving the flow characteristics within a complex geometry and able to

capture the viscous sublayer effects. Table 6 lists all flow physics enabled for simulation.

Table 6. Fluid physics enabled with accompanying model.

Physics	Enabled Model
Space	Three Dimensional
Time	Steady
Flow	Segregated
Equation of State	Constant Density
Viscous Regime	Turbulent
Gradient Method	Hybrid Gauss-LSQ
Wall Treatment	Two-Layer All y^+
k-ε Turbulence Model	Realizable k-ε Two-Layer

A few test cases were simulated to determine the number of iterations needed for

the solutions to converge. The solutions converged before 2000 iterations. Based on this

data, all test cases were simulated for 2500 iterations for the solution to converge. The

flow properties were set to be the exact same properties from the experiment. The

models were simulated on Texas A&M's Ada supercomputer. The university allocated

200,000 Service units (SUs) for the project. SU's represent units of time on the Ada

server. One SU is equal to 1 CPU hour on the platform.

The single cubic unit cells were also simulated in ANSYS Fluent. ANSYS Fluent

provides a rich framework to model fluid flow and heat transfer. It is one of the leading

commercial codes in academia and industry and continues to expand its use on many

applications. To verify the Star CCM+ pressure drop solutions, a single unit cell was

modeled in ANSYS Fluent with the exact same boundary and inlet conditions, physics models, and mesh as in Star CCM+. The structured mesh was used in all cases.

2.2.1.4 Boundary and Initial Conditions

Boundary conditions were specified on all solution domain boundaries. A total of four boundaries were applied to the fluid region. Figure 12 demonstrates the flow direction through the fluid with an established coordinate system. A velocity inlet condition was applied to the inlet surface, and a pressure outlet condition was applied to the outlet surface. The turbulence specification for both of these boundaries were fixed at intensity and length scale. The length scale was calculated using Eq. (2.3),

$$l = 0.038 d_h \qquad (2.3)$$

Where d_h is the hydraulic diameter of the unit cell inlet fluid face. The hydraulic diameter was calculated for each unit cell with Eq. (2.4),

$$d_h = \frac{4A}{P} \qquad (2.4)$$

Where A is the area and P is the perimeter of the inlet unit cell face. An example representation of the inlet unit cell area and perimeter displayed in Figure 13 for the Cubic40 model. Symmetry planes were applied to the negative x and negative y-surfaces to reduce computation time. The remaining surfaces were set as wall.
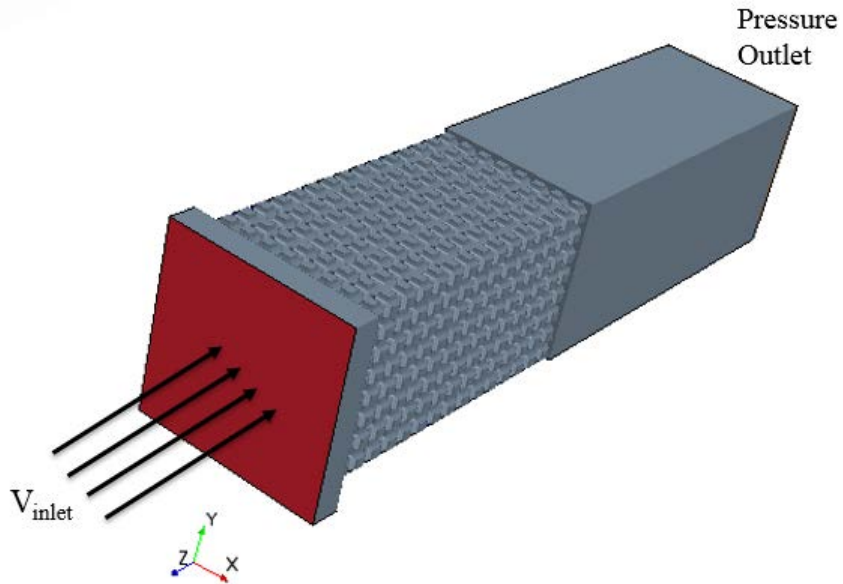
Figure 12. Flow direction through the fluid using a quarter symmetric domain.
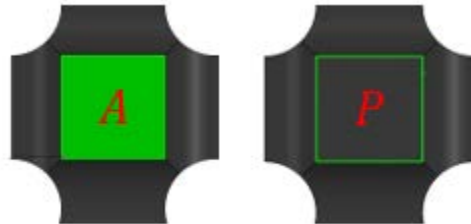
Figure 13. Unit cell inlet area (*A*) and perimeter (*P*) for the Cubic40 model used to calculate the hydraulic diameter (d_h).

All models were simulated with 12 different initial velocities ranging from 0.83 to 5.83 m/s. The experimental velocity and turbulence intensity curve fits were mapped to the inlet surface for each case. The velocity profiles were normalized to a value of 1, so that the profiles could simply be multiplied by an average entrance velocity condition. The velocity profiles at 2, 5, 8, and 10 SCFM were interpolated for each velocity condition. This was accomplished by first organizing the velocity data in to a single

vector, which included the velocity in the vertical and diagonal directions, along with a value of zero along the wall. Two positions vectors, one for the x-coordinate and another for the y-coordinate, were created that corresponded to the velocity position. The scatteredInterpolant function in MATLAB performs interpolation on a 2-D data set of scattered data. The returning function can then be evaluated at a set of points. The velocity and coordinate vectors were used to create an interpolation function for a single quadrant of a full scale model. Then, cell centroid positions of the inlet surface of a meshed model were imported into MATLAB as a CSV file. The file passed through the scatteredInterpolant function, and a corresponding velocity was attached to a cell centroid.

The same process was done for the turbulence intensity profile. First, the turbulence intensity at each anemometer location was calculated by using Eq. (2.5),

$$I = \frac{u'}{U} \tag{2.5}$$

where u' is the standard deviation of the velocity signal, and U is the mean velocity. A scatteredInterpolant function was created, and the cell centroids of the meshes were inputs. A CSV file was created and returned the x and y coordinates of each cell centroid with its velocity in the u, v, and w-directions along with the turbulence intensity. In this problem, the velocities in the u and v-directions were set to zero. The CSV file was imported into Star CCM+, and the flow field was initialized with velocity and turbulence intensity conditions.

27

2.2.2 Heat Transfer

The second half of the numerical analysis was to gather heat transfer data. In order to accomplish this, the solid must be modeled in conjunction with the fluid. A half-scale model was developed to determine the number of SUs needed. The model consisted of approximately 20 million tetrahedral elements. This would have been the standard fine mesh size for all half-scale models. It took 10 hours to generate the mesh on a local 8-core computer. The simulation was uploaded to Ada, and the solution converged at around 17,000 iterations. The same simulation was simulated for 25,000 for conservatism and occupied approximately 800 SUs. It was determined that a 1 x 8 x 8 unit cell lattice would be modeled to reduce element count and computational time. Figure 14 shows the 1 x 8 x 8 CAD model for the solid and fluid of the Cubic20 sample. A 1.5 in inlet and outlet channel were attached to both sides of the models.
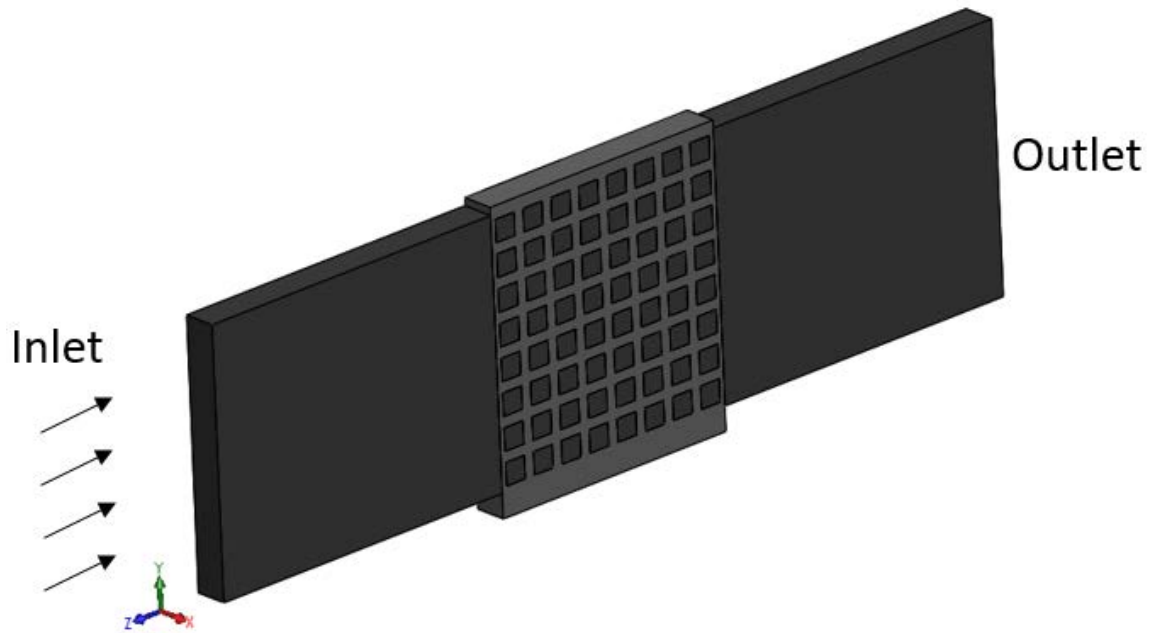
Figure 14. 1 x 8 x 8 lattice comprised of the Cubic20 unit cell.

2.2.2.1 Meshing

Complications can arise when two meshes of different materials or parts are joined together. The intersection between two elements may not end up being a sub-element of both. This can occur with a face, an edge, or a node. The shared element of two meshes also may not be complete. For this reason, conformal meshing is a recommended meshing method to avoid having these problems. Conformal meshing means that two meshes are consistent with every pair of adjacent elements and can intersect only at an edge or point. Although non-conformal meshes can be reliable, conformal meshes were generated between the fluid and solid regions to avoid problems for later implementation.

Conformal meshing was successfully generated using the meshing tools in Star CCM+ for the cubic models, but failed to generate conformal mesh for the remaining models. This is due to the complex geometry of the octet, diagonal, and midpoint unit cells at the fluid and solid interface. An alternative meshing software was used to successfully generate conformal mesh for all models. ANSYS Workbench is a platform that integrates ANSYS analysis tools such as solid mechanics and fluid dynamics.

The Geometry and Mesh component systems were implemented into the Workbench platform. The 1 x 8 x 8 SolidWorks CAD models were imported to ANSYS Design Modeler, which is another CAD software. Here, the fluid and solid faces were distinguished. The models were imported to the meshing tool. Inflation (prism layers) was added to the fluid walls with the same parameters as the pressure drop models. Unstructured tetrahedral conformal meshes were generated for all models. Figure 15 shows the conformal mesh for the Cubic60, and Table 7 lists the mesh element counts.
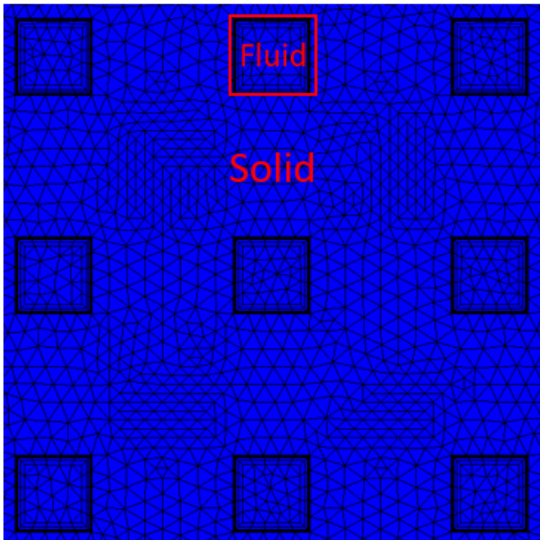
Figure 15. Side view of the Cubic60 fine conformal mesh with nine unit cells and the surrounding solid.

Table 7. Unstructured mesh element counts for 1 x 8 x 8 models.

	Number of Mesh Elements		
Sample	Coarse (million)	Medium (million)	Fine (million)
Cubic20	2.13	3.54	5.23
Cubic40	1.98	3.24	4.72
Cubic45deg	2.65	4.12	6.21
Cubic60	2.02	3.15	4.64
Diagonal40	2.24	3.47	5.03
Midpoint40	2.17	3.55	4.85
Octet40	2.45	3.81	5.79

As with the pressure drop models, a structured and unstructured mesh of a single cubic unit cell was generated. Structured meshing was done in ICEM CFD with hexahedral cells, while unstructured meshing was completed in Star CCM+ with polyhedral cells. Both meshes used conformal meshing. Figure 16 shows the two types of meshes and Table 8 lists the mesh element counts.
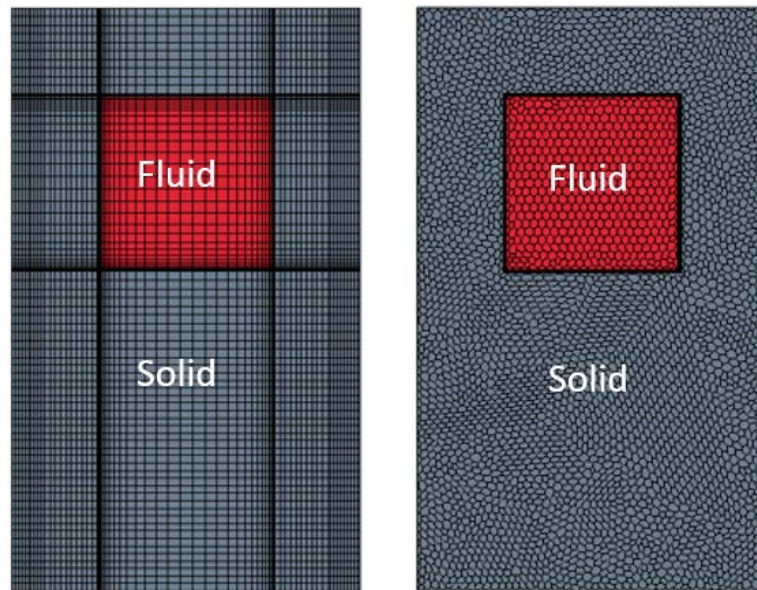
Figure 16. Structured (left) and unstructured (right) meshes of the Cubic40 solid and fluid unit cell.

Table 8. Total element counts for the unstructured and structured single unit cell solid and fluid meshes.

Sample	Unstructured Element Count			Structured Element Count		
	Coarse	Medium	Fine	Coarse	Medium	Fine
Cubic20	121100	217300	375000	126000	212000	385000
Cubic40	123900	211300	377800	126000	212000	385000
Cubic60	122400	209600	385400	126000	212000	385000

2.2.2.2 Simulation Setup

The same fluid physics models from the pressure drop models was applied to the fluid of the heat transfer models. A case was carried out to observe the change in temperature to determine if constant density could be applied throughout the solid or if it needed to be a function of temperature. The case was simulated at the highest velocity condition, and the temperature increased by 50 K. It was concluded that the temperature difference was small enough that a solution with constant density wouldn't lose significant accuracy. Therefore, constant solid density was applied to all models. Table 9 shows the solid physics models enabled for all cases. The segregated solid energy model allowed the heat to transfer from fluid to solid. The fluid and solid properties were set to the experimental properties.

Table 9. Sold physics enabled with accompanying model.

Physics	Enabled Model
Space	Three Dimensional
Time	Steady
Equation of State	Constant Density
Gradient Method	Hybrid Gauss-LSQ
Other	Segregated Solid Energy

Another test case was created to determine the number of iterations needed to reach convergence. The test case converged at approximately 16,000 iterations with

residuals as low as 10^{-4}. All cases were set to simulate for 25,000 iterations for conservatism. The heat transfer cases were simulated on the Ada supercomputer.

As done with the pressure drop unit cell models, the heat transfer unit cell models were repeated with ANSYS Fluent. The fluid and solid physics models were set equal to the Star CCM+ physics models. All coefficients, schemes, and input conditions were equal. The structured mesh remained the same across each CFD software. Only the Cubic20, Cubic40, and Cubic60 unit cells were modeled.

2.2.2.3 Boundary and Initial Conditions

Boundary conditions were specified for the fluid and solid regions. The fluid region had a velocity inlet type at the inlet surface and a pressure outlet type at the outlet surface. Symmetry conditions were applied in the positive and negative-x surfaces. The remaining faces were set as walls. For the solid, symmetry conditions were also applied in the positive and negative x-surfaces. The remaining faces were set as adiabatic walls, except the bottom surface, which was fixed at a constant heat source of 60.4 W (7.55 W for 1 x 8 x 8 models). A contact surface was created where fluid and solid walls met. A contact interface boundary was specified at the contact surface to allow the heat transfer to pass from the solid to the fluid. Figure 17 displays the flow and heat direction through the 1 x 8 x 8 models.
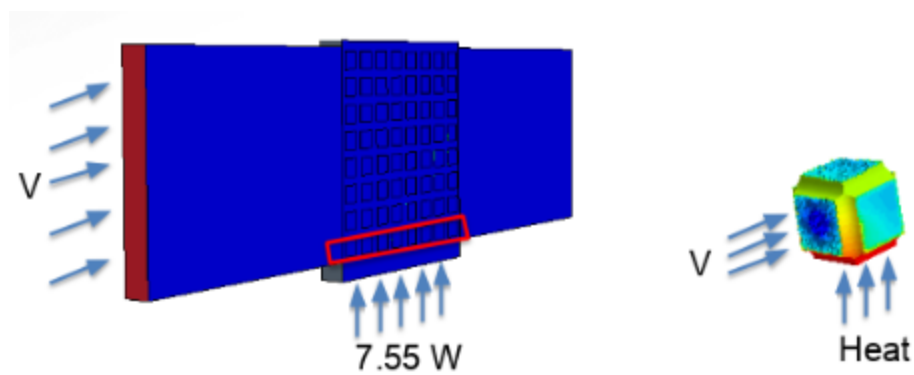
Figure 17. Flow and heat direction for the 1 x 8 x 8 and single unit cell models.

The experimental velocity and turbulence profiles were mapped to the inlet surface in the same manner as the pressure drop models. Although the pressure drop models were simulated at 12 velocity conditions, only 5 were simulated for the heat transfer models due to computational time constraints. These velocity conditions also ranged from 0.83 to 5.83 m/s.

2.2.3 Post-Processing

Star CCM+ has several post-processing tools to visualize and analyze results from a simulation. One of these tools is scene creation, which allows the model to be visualized. Scalar and vector scenes were created to view scalar fields and vector fields, respectively. Derived parts, such as surfaces, lines, and streamlines, were viewed in these scenes to focus on a specific model location or area.

One of the disadvantages of post-processing in Star CCM+ is the limitations of plot formatting. Therefore, all plots were created and formatted in MATLAB. XYZ internal tables were created in Star CCM+ to create an empty xyz tabular data set. These

tables were filled with data extracted from specified scalar functions for a given part. The extracted CSV files were read in MATLAB where the data could be further analyzed.

To analyze the pressure drop across the samples, a surface averaged report was created at the inlet surface. Star CCM+ calculates the surface average using Eq.(2.2),

$$P = \frac{\sum_i P_i A_i}{\sum_i A_i} \qquad (2.2)$$

Where P_i is the cell centroid pressure and A_i is the cell center area. The pressure drop was correlated as a function of Reynolds number (Re). Reynolds number as a function of unit cell velocity was found by Eq.(2.3),

$$Re = \frac{\rho_{air} V_{uc} d_{uc}}{\mu} \qquad (2.3)$$

Where V_{uc} is the unit cell velocity, μ is the kinematic viscosity of air and ρ_{rel} is the unit cell relative density. To be consistent with the experimental pressure drop results, Re was altered to be a function of average channel velocity. Through mass flow rate manipulations in the channel, the unit cell velocity was found to be

$$V_{uc} = \frac{V_{avg}}{1 - \rho_{rel}} \qquad (2.4)$$

Where V_{avg} is the average channel velocity and ρ_{rel} is the unit cell relative density. Substituting Eq. (2.4) in Eq. (2.3) yields Eq. (2.5) resulting with Re as a function of unit cell relative density (ρ_{rel}) and geometry (d_{uc})

$$Re = \frac{\rho_{air} V_{avg} d_{uc}}{\mu(1 - \rho_{rel})} \tag{2.5}$$

To analyze the heat transfer from a model, fluid and solid scalars were exported to a CSV file. For the fluid, each cell centroid coordinates were extracted with their accompanying volume and temperature. For the solid, the cell centroid coordinates were extracted with their accompanying area, boundary heat flux, and temperature. Although the pressure drop calculations were completed in Star CCM+, the heat transfer calculations were completed in MATLAB.

The solid and fluid cells were separated into unit cells based on the centroid coordinates. The bulk temperature of the fluid per unit cell was calculated by taking a volume average. This was calculated using Eq. (2.6)

$$T_{bulk} = \frac{\sum_i T_{f,i} V_{f,i}}{\sum_i V_{f,i}} \tag{2.6}$$

Where $T_{f,i}$ is the cell temperature and $V_{f,i}$ is the cell volume. The heat transfer coefficient per unit cell was calculated with Eq. (2.7),

$$h = \frac{\sum_i \frac{Q_i A_{s,i}}{T_{s,i} - T_{bulk}}}{\sum_i A_{s,i}} \tag{2.7}$$

where Q_i is the cell boundary heat flux, $A_{s,i}$ is the solid cell are, and $T_{s,i}$ is the solid cell temperature. By knowing the heat transfer coefficient, Nusselt number was found with Eq. (2.8)

$$Nu = \frac{hd_{uc}}{k_f} \qquad (2.8)$$

Pressure drop and Nusselt number correlations were formed as a function of Re.

Pressure drop was non-dimensionalized by dynamic pressure. The curve fitting tool in

MATLAB returned the curve fit coefficients for each correlation. The correlations were

then used to optimize the lattice. Finally, the correlations were sent to a colleague at the

University of Pittsburgh, who optimized the lattice based on structural and fluid

performance data.

CHAPTER 3

PRESSURE DROP RESULTS

3.1 Numerical Data

The full model pressure drops of each unit cell geometry were almost identical to

the quarter symmetric model pressure drops. All models resulted in a pressure drop

difference of less than 0.06%. As a result, quarter symmetric models were developed and

simulated to reduce computational cost while still mainting accurate solutions. The

numerical pressure drop data was compared to one another according to three criteria:

unit cell relative density (Figure 18), geometry (Figure 19), and orientation (Figure 20).
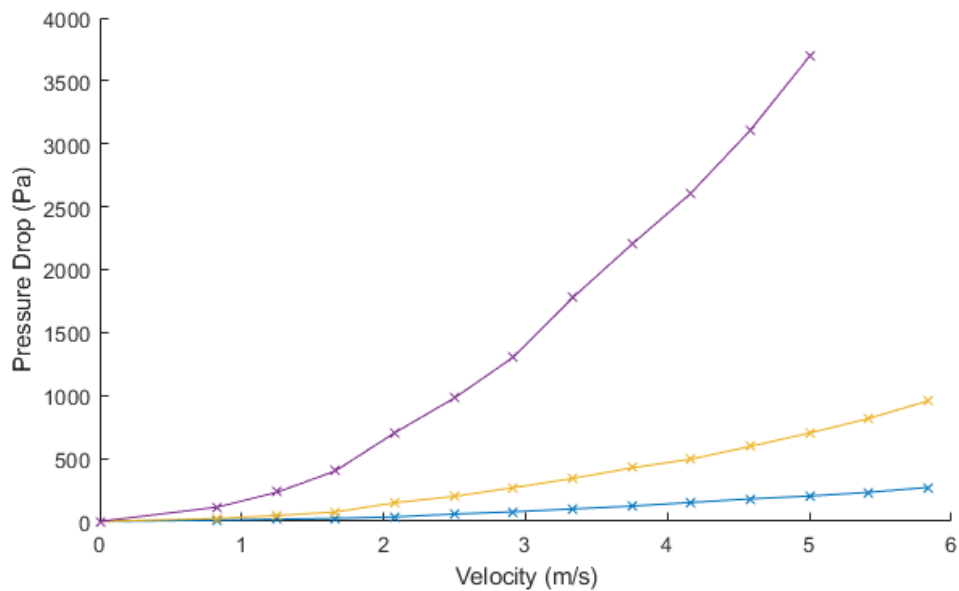
Figure 18. Numerical pressure drops according to unit cell relative density (quarter
symmetric models).

The pressure drop results of the three cubic lattices of different relative densities

proved that relative density is a factor that greatly influences pressure drop. An example

of the effect relative density had on pressure drop was analyzed at a velocity of 1.8 m/s.

Numerically, the pressure drop increased by a factor of 4.2 from the Cubic20 to Cubic40

samples and by a factor of 5.2 from the Cubic40 to Cubic60 samples. Similarly, the

experimental pressure drop increased by a factor of 4.7 from the Cubic20 to Cubic40

samples and by a factor of 6.8 from the Cubic40 to Cubic60 samples. Large ligament

diameters cause a greater pressure drop as they create more obstruction in the flow. A

similar trend would be expected for other unit cell geometries at different relative

densities.
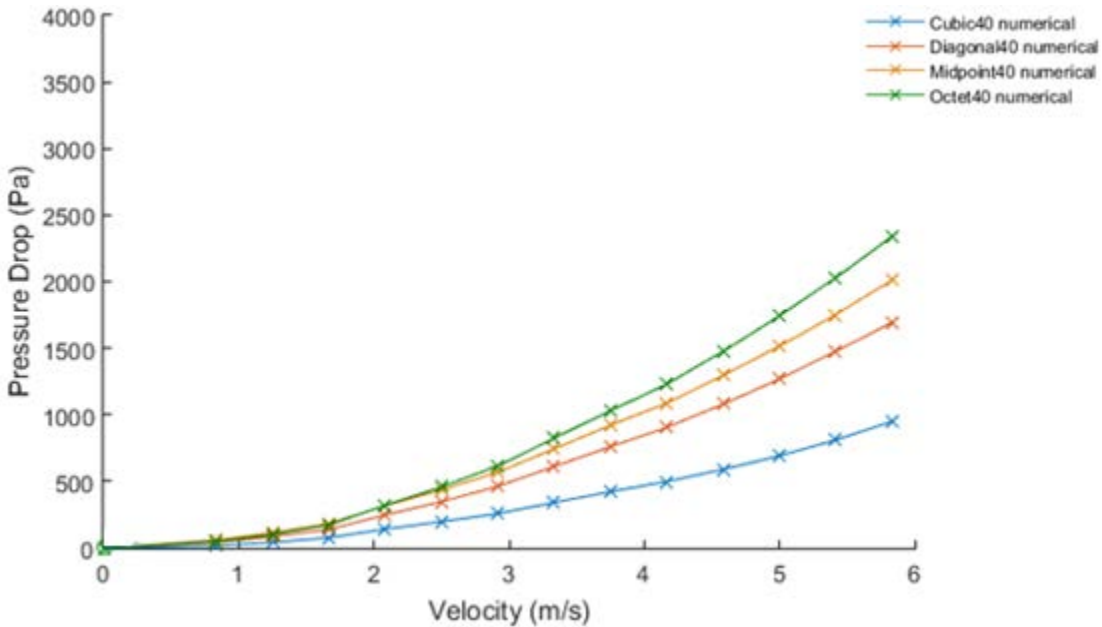
Figure 19. Numerical pressure drops according to unit cell geometry.

The Octet40 sample had the highest pressure drop according to unit cell geometry followed by the Midpoint40, Diagonal40, and Cubic40 samples. Although these four samples were manufactured to have the same relative density, the tortuosity of the fluid path inside each unit cell was different. This caused each sample to have a different pressure drop. The flow path required in the Octet40 represents the least direct route, and therefore experienced the highest pressure drop. This sample also had the most ligaments of any unit cell. A single octet, midpoint, diagonal, and cubic unit cell comprised of 32, 28, 20, and 12 ligaments, respectively. More ligaments in a unit cell create more resistance to fluid flow. As expected, the less free path the fluid experiences, the greater the pressure drop.
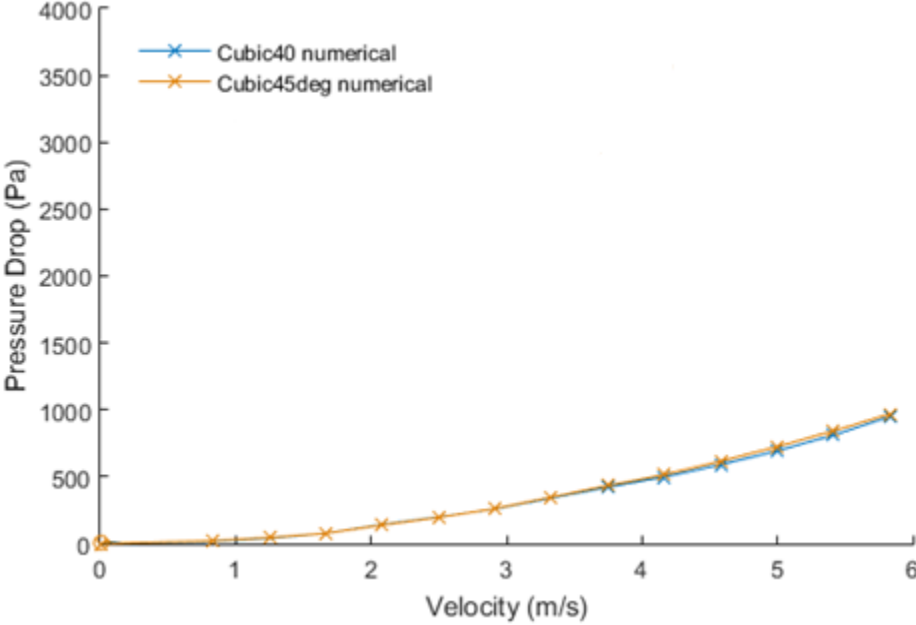
Figure 20. Numerical pressure drops according to unit cell orientation.

Finally, the effect of unit cell orientation was analyzed by comparing the pressure drops of the Cubic40 and Cubic45deg samples (see Figure 22). The experimental

40

pressure drops between the two samples showed a clear distinction, whereas the numerical pressure drops showed little difference. According to the previous pressure drop explanations, number of unit cell ligaments and clear flow path visibility through the sample affect pressure drop. The Cubic40 and Cubic45deg samples had the same number of ligaments but different flow path visibility. By looking directly through the Cubic45deg sample, there is visibly less fluid flow free path than through the Cubic40 sample. Based on the numerical pressure drop results, orientation does not affect the pressure enough to be considered in designing a lattice structure. The difference in pressure drops was less than 1% at high velocities.

To quantify the numerical uncertainty, a Grid Convergence Index (GCI) method pioneered by Roache [19] was implemented in this study. The method involved performing a simulation on three successfully finer grids. As the grid is refined (grid cells become smaller and the number of cells in the flow domain increase) the spatial and temporal discretization errors should asymptotically approach zero. GCI was conducted at the highest velocity conditions for each model and the associated error was applied for each velocity condition for conservatism. 0 shows this numerical uncertainty. The Octet40 sample had the highest numerical uncertainty of 4.84%, and the Cubic20 had the lowest at 0.08%. This is due to the difficulty in nature of meshing complicated geometries such as the diagonal, midpoint, and octet unit cells. The uncertainty of input parameters such as length scale, velocity profiles, and turbulence intensity were also calculated, but were small enough to disregard.

Table 10. Pressure drop GCI uncertainty for the 8 x 8 x 8 models.

Sample	GCI (%)
Cubic20	1.39
Cubic40	1.55
Cubic45deg	2.67
Cubic60	2.98
Midpoint40	3.42
Diagonal40	2.83
Octet40	4.84

Pressure drop correlations were formed according to the numerical data. The pressure drop was non-dimensionlized by dynamic pressure. The correlations were functions of Re following the form of Eq.(3.1),

$$\frac{\Delta P}{\frac{1}{2}\rho_f V_{avg}^2} = a\,\text{Re}^b \tag{3.1}$$

where *a* and *b* are the curve fit coefficients. Table 11 lists the curve fit coefficients for the 8 x 8 x 8 numerical pressure drop models. The correlations were formed for a low velocity regime and a high velocity regime. The transition from laminar to turbulent flow occurred at approximately 1.8 m/s.

Table 11. Pressure drop curve fit coefficients for 8 x 8 x 8 models.

Sample	Low Velocity Regime		High Velocity Regime	
	a	b	a	b
Cubic20	7.6	0.06	32.3	-0.13
Cubic40	19.4	0.15	84.3	-0.08
Cubic45deg	62.7	-0.13	123.3	-0.12
Cubic60	485.8	-0.12	329.8	-0.04
Midpoint40	272.1	-0.19	185.9	-0.07
Diagonal40	567.4	-0.31	136.8	-0.06
Octet40	1070.0	-0.39	266.6	-0.14

3.2 Single Unit Cell

A pressure profile was analyzed through a single channel of each model. Figure 21 shows the numerical pressure across the Diagonal40 model at 3.33 m/s. A line probe was created through a row of unit cells near the centerline of the flow (bottom row of Figure 21). The row of unit cells analyzed was consistent for each model. Figure 22 shows the pressure through a row of the Cubic40 model at 5 m/s as a function of row distance. The vertical lines represent the start of a unit cell. The pressure drop per unit cell (Table 2) was calculated by taking the difference of the average surface pressure at the inlet and outlet unit cell surfaces. The pressure drop per unit cell reached close to a steady state after the third unit cell. This was the case for all models with different unit cell geometries or relative densities. After the third unit cell, the pressure drop changed by less than 3.5% with the subsequent unit cells. The computational time can be reduced by modeling the first four unit cells of a lattice. The pressure drop for the fourth unit cell can then be subsequently added to the desired number of remaining unit cells in the domain for a total pressure drop.
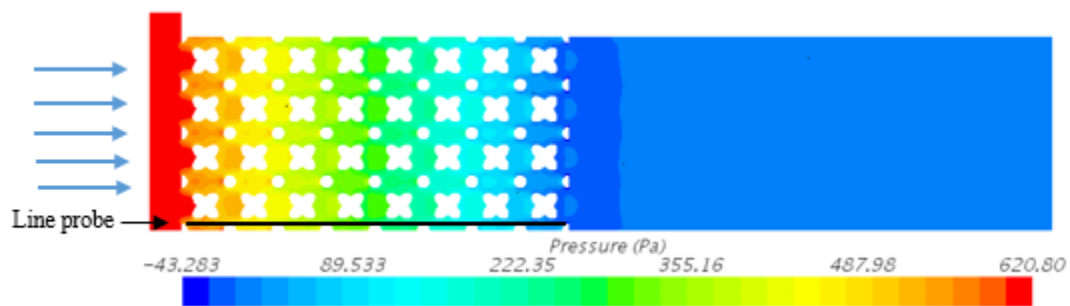
Figure 21. Numerical pressure drop across the Diagonal40 model at 3.33 m/s.
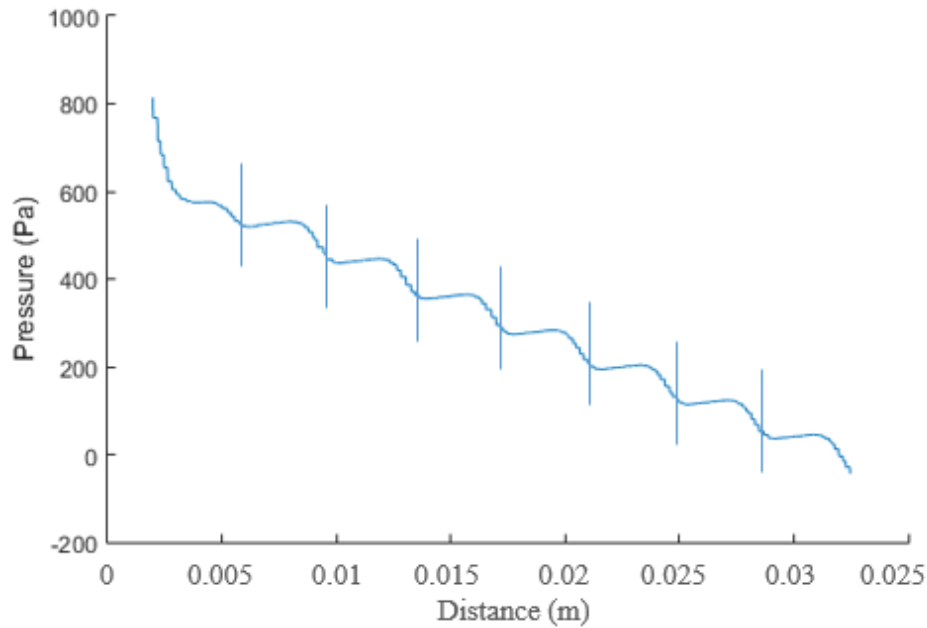
Figure 22. Pressure through a row of the Cubic40 model at 5 m/s. Each vertical line represents the start of a unit cell.

Table 12. Pressure drop per unit cell of the Cubic40 model at 5 m/s.

Unit Cell	Pressure Drop (Pa)	Percent Different From Previous Unit Cell (%)
1	238.45	
2	43.89	443.29
3	84.81	48.25
4	81.96	3.48
5	81.64	0.39
6	79.54	2.64
7	79.91	0.46
8	78.66	1.59

3.2.1 Structured vs Unstructured Mesh

The meshes of the three cubic unit cells of different relative densities were generated both structurally and unstructurally for a single unit cell to analyze the tradeoff between pressure drop accuracy and grid generation time. Figure 23 shows the pressure

44

drop comparison using the two meshing strategies. The change in pressure drop using a structured mesh compared to an unstructured mesh was minimal. The change in pressure drop is greatest at higher velocities. The Cubic60 unit cell had the greatest change in pressure drop, but only by a 2.2% difference. A representation of the pressure between the two meshing strategies for the Cubic60 single unit cell is displayed in Figure 24.
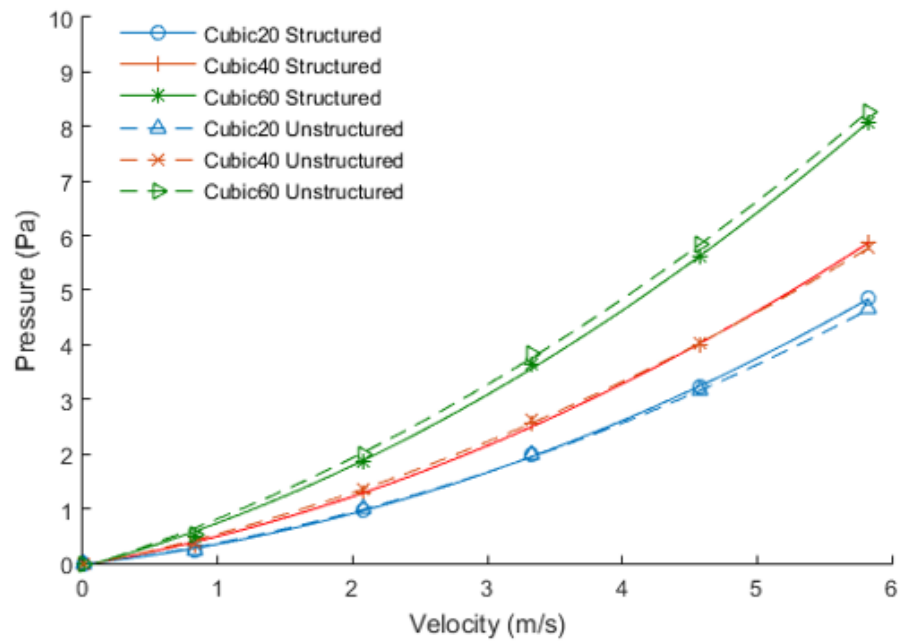
Figure 23. Pressure drop comparison of structured and unstructured mesh for the cubic unit cells.
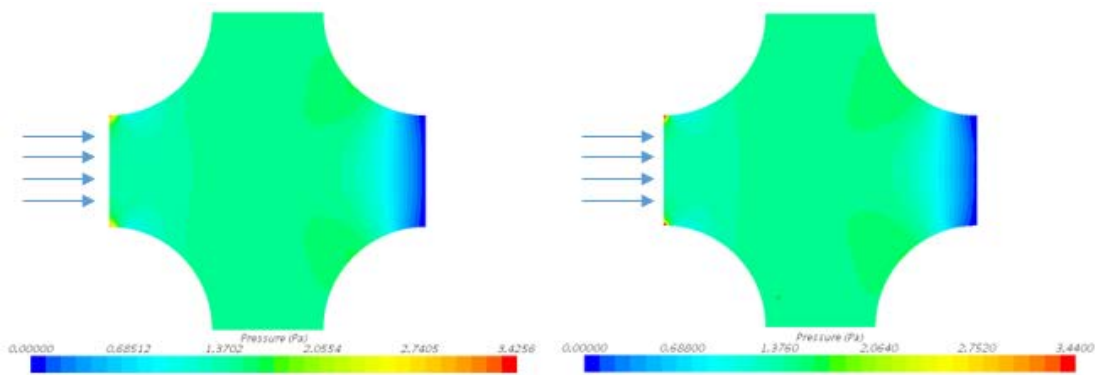
Figure 24. Pressure comparison for the Cubic60 single unit cell models using a structured mesh (left) and an unstructured mesh (right).

One of the benefits of structured meshes was the fast convergence rate for the models. On average, the solutions with structured mesh converged 30% faster than those with unstructured meshes. The numerical uncertainty was also lower for structured meshes. Table 13 lists the GCI uncertainty for both mesh types at the highest velocity. The numerical uncertainty of the structured meshes was between 250-425% less than the unstructured meshes.

Table 13. Pressure drop GCI uncertainty comparison of structured and unstructured mesh for the cubic unit cells.

Sample	Unstructured GCI (%)	Structured GCI (%)
Cubic20	1.23	0.35
Cubic40	1.83	0.42
Cubic60	2.02	0.63

It is difficult to quantify mesh generation time for structured meshes, as that depends significantly on the user's knowledge and efficiency of mesh generation software. One of the difficult steps in creating structured meshes in ICEM CFD is the

46

blocking strategy to discretize the domain for nodal specification. The cubic unit cells only needed 7 blocks to successfully generate a mesh. However, the other unit cell geometries would need a unique blocking strategy to generate a good quality mesh.

Although structured meshes favor faster convergence and lower pressure drop uncertainty, the unstructured meshes provided acceptable pressure drop results. For this reason, unstructured meshes were generated for the quarter symmetric models in the previous section to compare to the experimental pressure drops. Unstructured mesh generation was significantly faster than structured mesh. The time it took to generate a structured mesh outweighed the time saved on faster solution convergence. Therefore, if time is the biggest factor, it is recommended to model pressure drop with unstructured meshes. If accuracy is critical, it is recommended to model pressure drop with structured meshes. Since the difference in pressure drop between the two meshing strategies is minimal, it is recommended to generate unstructured meshes for unit cells of complex geometry.

3.2.2 Star CCM+ vs ANSYS Fluent

The cubic single unit cells with fine structured meshes were simulated in ANSYS Fluent with the same boundary and inlet conditions as the models in Star CCM+. The same flow physics models were the same for both cases. Figure 25 shows the pressure drops of the single cubic unit cells for both CFD software.
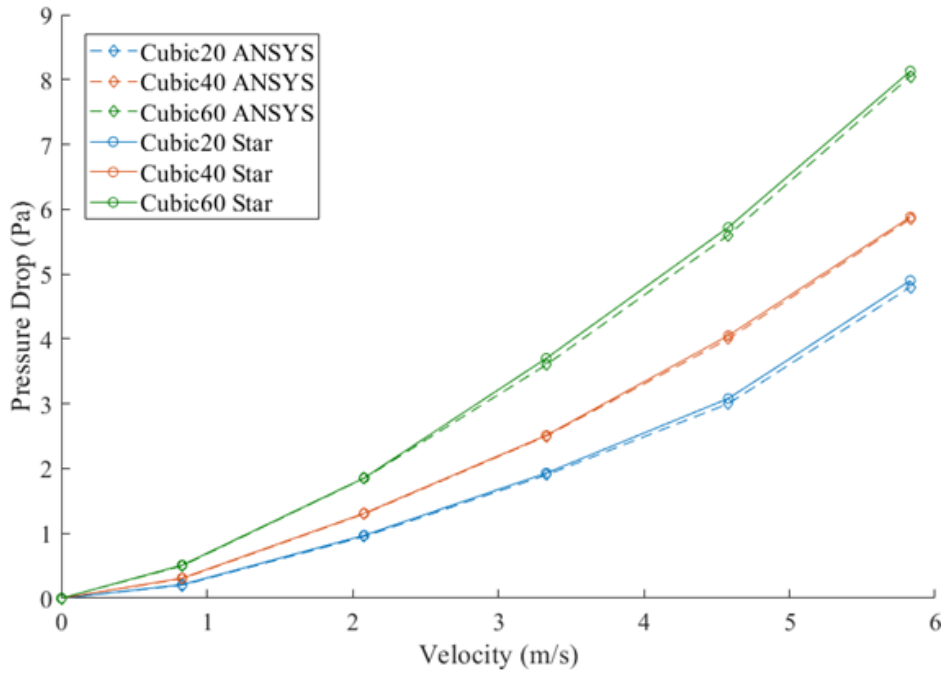
Figure 25. ANSYS Fluent vs. Star CCM+ cubic unit cell pressure drops using fine structured mesh.

It was expected that the pressure drops would be exactly the same if the conditions and physics models were identical. The cubic models in Star CCM+ resulted in a slightly greater pressure drop than the models in ANSYS Fluent. The difference in pressure drop increased as velocity increased. However, the pressure drop at 5.83 m/s only differed 0.19% between the two CFD softwares. The slight difference in pressure drops between the two CFD softwares is most likely contributed to the wall functions that were selected. The wall functions for both codes were for a near wall thickness $y+ <$ 1. For this wall thickness, Star CCM+ uses a wall treatment that blends near and far wall and is more flexible in terms of cell size. A thorough investigation in the pressure drop difference was not conducted since the difference is minimal.

Convergence time was also explored between the two CFD codes. The study was conducted for the Cubic20 at 5.83 m/s, since this is the sample with the most fluid at the highest velocity condition. The convergence threshold was the point at which the residuals reached a steady state value or below 10^{-4}. The Cubic20 model converged in 478 iterations in Star CCM+ and 468 iterations in ANSYS CFD. The difference in the 17 iterations for this size mesh is less than a second of computation time on the average computer. It is concluded that either of the two CFD software is more than capable of solving an accurate pressure drop across the cubic samples. Since neither CFD code showed an advantage over the other, it is recommended that the software one is most experienced with is selected.

CHAPTER 4

HEAT TRANSFER RESULTS

The difference in numerical and experimental pressure drops across the samples differed by an order of magnitude. The experimental thermal data did not seem as trustworthy since the losses were extremely high. When trying to account for these losses, the experimental uncertainty in the thermal resistance became quite large. As a result, the experimental heat transfer data will not be compared to the numerical heat transfer data.

4.1 Numerical Data

Much like the pressure drop data, the heat transfer data was analyzed based on unit cell relative density, unit cell geometry, and unit cell orientation. This was accomplished by first calculating the Nusselt number for each unit cell for a total of 64 unit cells. The Nusselt number was then averaged across each row. Row specification is shown in Figure 26. The Nusselt number for rows 2-7 were similar, while rows 1 and 8 resulted in a lower Nusselt number. This is due to rows 1 and 8 having more surface area per unit cell. Nusselt number was calculated per row for each sample at every velocity condition. Two separate correlations were formed: one for the average of rows 2-7 and one for row 1, as it is coincident to the heated surface. An example of the difference in Nusselt number between the middle rows and top and bottom rows is displayed in Figure

27 for the Cubic40 sample at 4.83 m/s. The average Nusselt number for the middle rows was selected as the basis for criteria comparison.
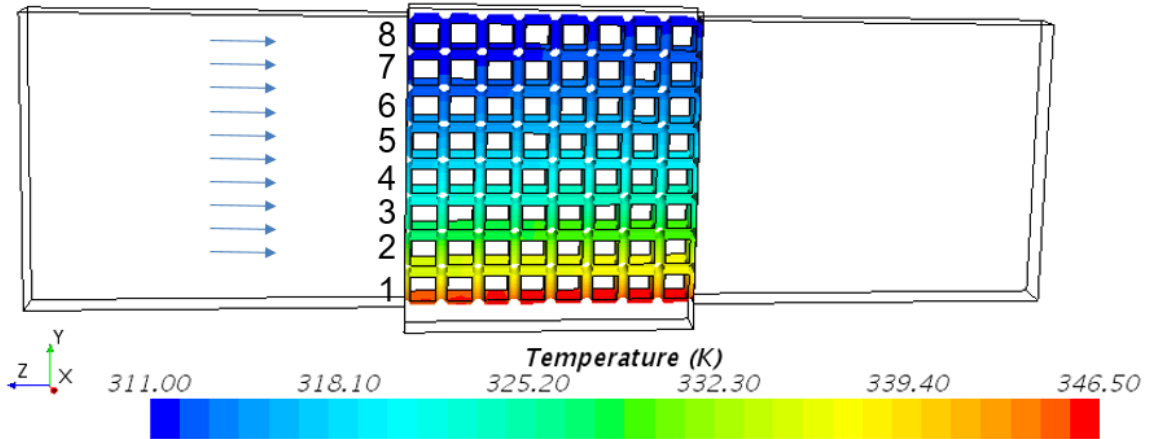
Figure 26. Nusselt number row specification
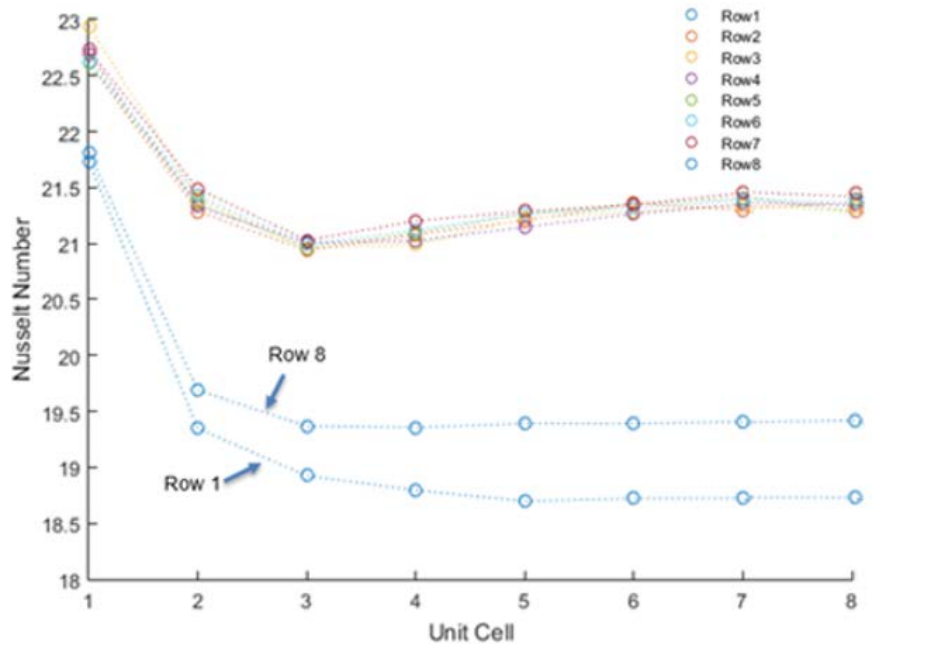
Figure 27. Unit cell vs Nusselt number for each row of the Cubic40 sample at 4.83 m/s.

According to unit cell relative density, the Cubic60 model had the highest
Nusselt number, followed by the Cubic40 and Cubic20 (see Figure 28). Nusselt number
was dependent on relative density. The trend was opposite to the pressure drop trend.
The Cubic20 sample resulted in the lowest pressure drop but also the lowest Nusselt
number. The difference in the amount of heat that was transferred from 20-40% and 40-
60% increased by an average factor of 1.5. Therefore, increasing the relative density of a
sample increases the Nusselt number in a non-linear fashion. An increasing velocity also
causes an increase in heat transfer performance, holding other variables constant.
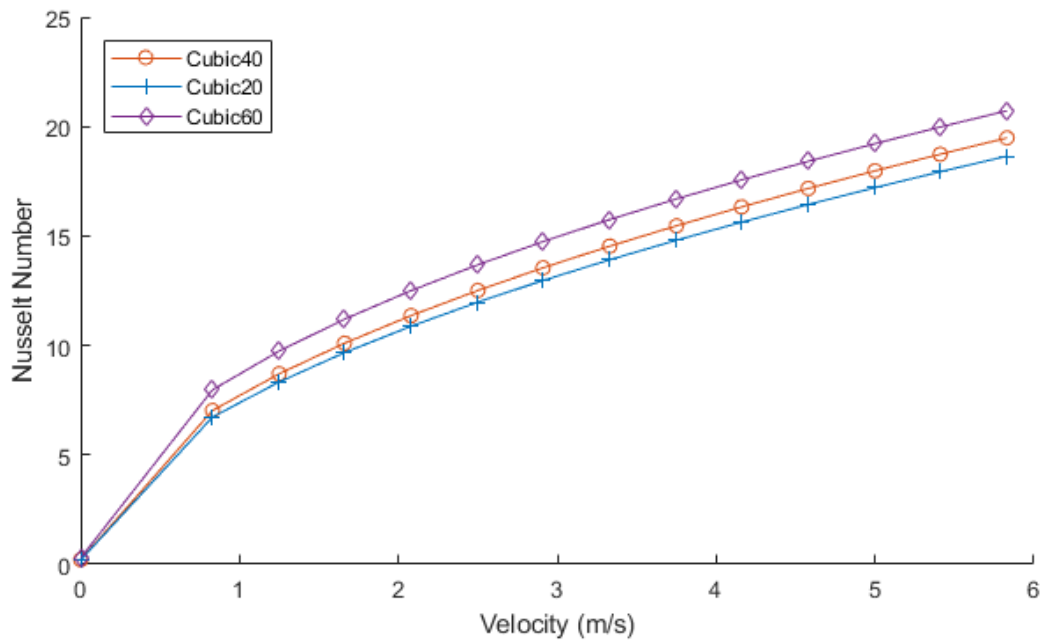
Figure 28. Nusselt number according to unit cell relative density.

Nusselt number based on unit cell geometry, as shown in Figure 29, was
significantly different across the four samples. The performance resulted in the

52

following order from highest to lowest Nusselt number: Diagonal40, Octet40, Cubic40, and Midpoint40. The Diagonal40 sample had about a 400% increase in Nusselt number compared to the Midpoint40 sample. The heat transfer trend did not show any similarities to pressure drop performance. It was expected that heat transfer would be proportional to number of unit cell ligaments due to the added surface area. The Octet40 had the most ligaments in a given unit cell, followed by Diagonal40, Midpoint40 and Cubic40. However, this trend was not the case. This is most likely due to flow obstruction. The Cubic40 and Midpoint40 samples had more free flow through the unit cells than the Diagonal40 and Octet40. The Diagonal40 and Octet40 samples caused significant flow disturbances, which created a longer path a fluid particle would travel. This allowed the flow to remove more heat than the other two samples. A side view of the temperature profile through the Octet40 model at 5.83 m/s is shown in Figure 30.
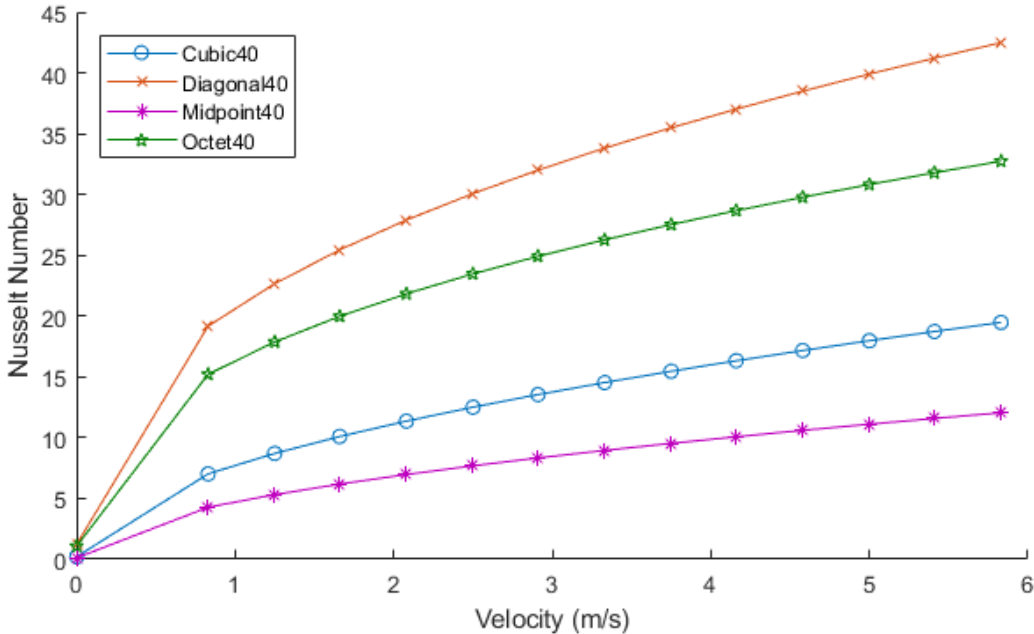
Figure 29. Nusselt number according to unit cell geometry
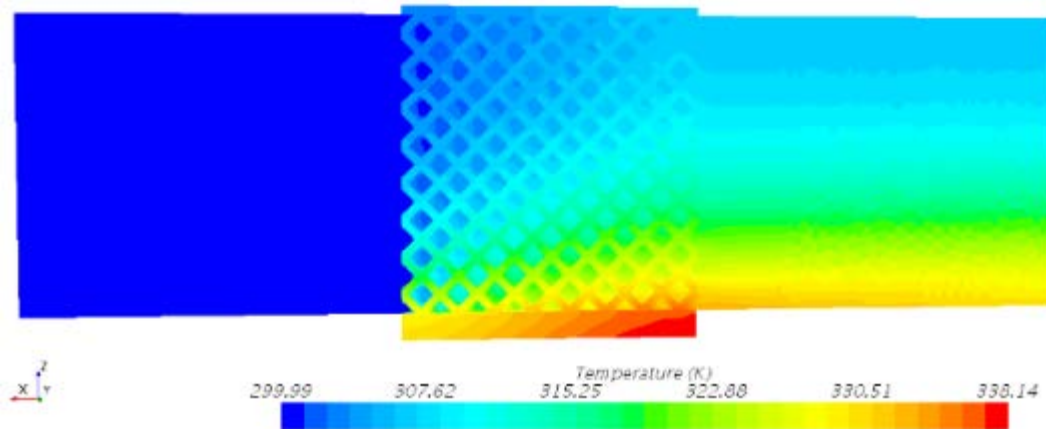
Figure 30. Temperature through the Octet40 model at 5.83 m/s.

Finally, heat transfer was analyzed according to unit cell orientation (Figure 31).
The Cubic45deg sample transferred heat slightly better than the Cubic40. The difference
in Nusselt number between the two samples was dependent on velocity. At higher
velocities, the Cubic45deg began to transfer heat about 1.15 times better than the
Cubic40 sample. It's important to recall that the pressure drops across these two samples
were almost identical. One sample did not produce a significant pressure drop over the
other. Therefore, designing a heat sink based on Cubic45deg unit cells should provide an
enhancement in thermal performance without a pressure penalty. The merit of rotating
other unit cells may or may not provide similar benefits. Additional samples would need
to be manufactured and tested.
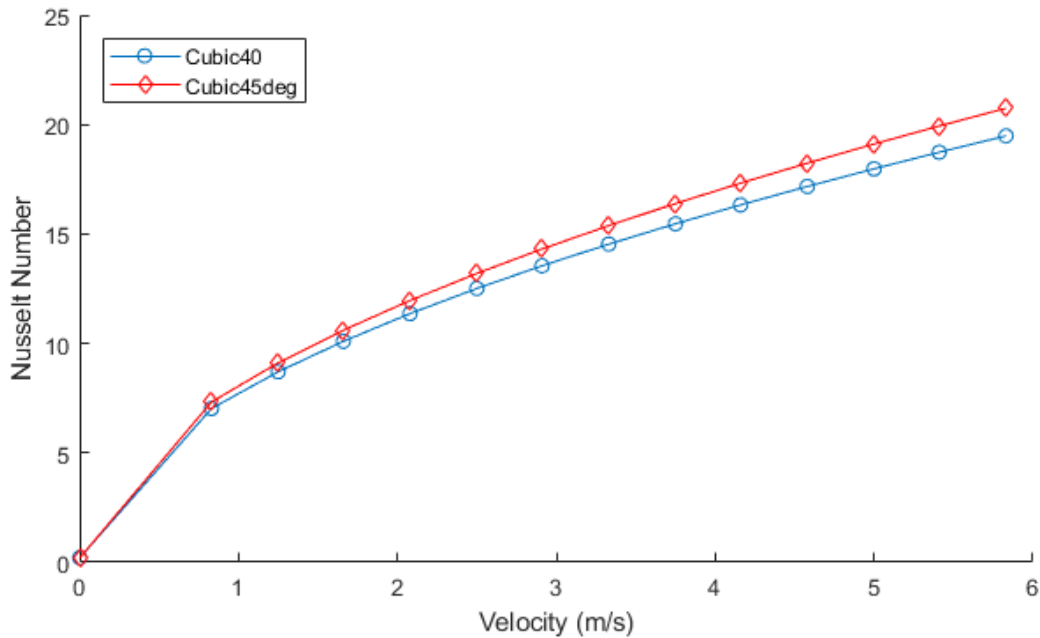
Figure 31. Nusselt number according to unit cell orientation.

Nusselt Number correlations were formed based on Equation (4.2)

An uncertainty analysis was performed to calculate the discretization error from mesh

generation. The same GCI method was used as in the pressure drop uncertainty analysis.

Table 14 lists the uncertainty due to mesh generation. The heat transfer uncertainty was

greater than the pressure drop uncertainty since both fluid and solid were being modeled.

The Octet40 has the highest uncertainty at 7.38% while the Cubic60 had the lowest at

2.87%. These uncertainties must be taken in to account when considering the

correlations that follow.

Table 14. Nusselt Number GCI uncertainty for the 1 x 8 x 8 models.

Sample	GCI (%)
Cubic20	4.25
Cubic40	4.02
Cubic45deg	3.98
Cubic60	2.87
Midpoint40	5.87
Diagonal40	6.46
Octet40	7.38

Nusselt number correlations were formed as part of the overall structural and thermal performance optimization. Two separate correlations were formed for the averaged middle rows and average first row. The correlations follow the form of Eq. (4.1). The coefficients are listed in Table 15.

$$Nu = aRe^b \qquad\qquad (4.1)$$

Table 15. Nusselt number curve fit coefficients for 1 x 8 x 8 models.

Sample	First Row		Middle Rows	
	a	b	a	b
Cubic20	0.332	0.561	0.481	0.523
Cubic40	0.394	0.537	0.460	0.523
Cubic60	0.565	0.493	0.634	0.480
Cubic45deg	0.284	0.531	0.334	0.534
Diagonal40	2.929	0.358	2.015	0.408
Midpoint40	0.480	0.510	0.424	0.531
Octet40	3.188	0.327	2.041	0.393

Figure 30 displayed the Nusselt number per unit cell for each row within the Cubic40 model. A similar trend per unit cell occurred for Nusselt number as it did for pressure drop. After about 3-4 columns, the fluid becomes fully developed, and the

Nusselt number reaches a constant value. It is recommended that for similar studies, only the first four columns need to be modeled in order to capture the entrance region heat transfer characteristics, after which a constant Nusselt number can be applied to all remaining columns.

4.2 Single Unit Cell

A single cubic unit cell was modeled from the Cubic20, Cubic40, and Cubic60 heat transfer models. The two different meshing styles, structured and unstructured, were analyzed. The models were also imported into ANSYS Fluent and the heat transfer results were compared to those modeled in Star CCM+. These comparisons are discussed in the following subsections.

4.2.1 Structured vs Unstructured Mesh

The meshes of the three cubic unit cells of different relative densities were generated both structurally and unstructurally for a single unit cell to analyze the tradeoff between heat transfer accuracy and grid generation time. A total of 60 W of power was supplied to the bottom of the unit cells. Figure 32 shows the Nusselt number for each meshing technique at various velocities. The change in Nusselt number between the two meshing styles was more noticeable than the change in pressure drop. All three cubic unit cells had roughly a 9% difference in Nusselt number. Figure 33 displays the temperature through a Cubic20 unit cell at 0.83 m/s using the fine mesh.
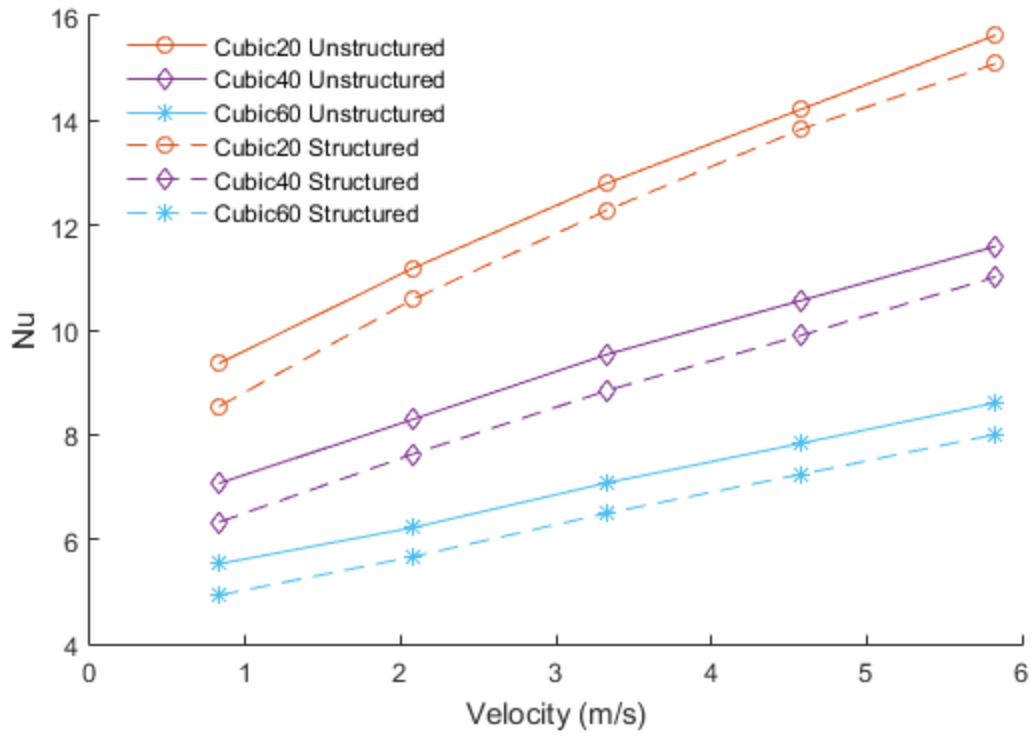
Figure 32. Nusselt number comparison of structured and unstructured mesh for the cubic unit cells.
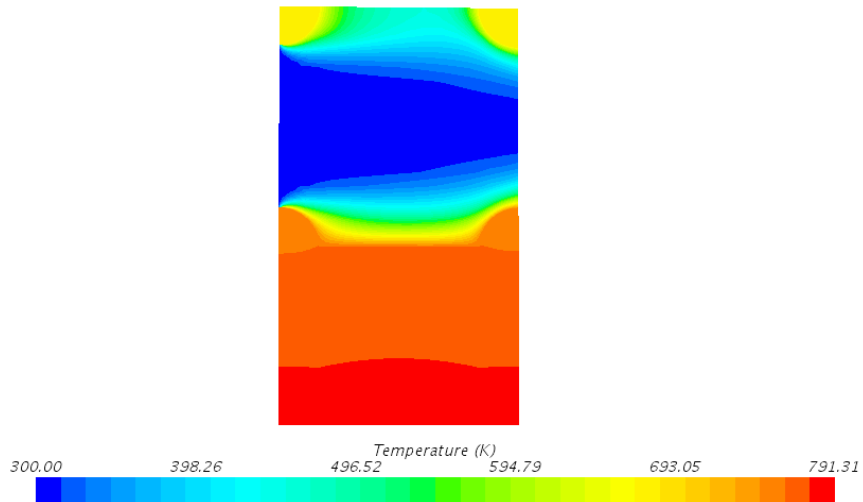

Figure 33. Temperature through Cubic20 unit cell at 0.83 m/s

The models with structured meshes on average converged roughly 40% faster than the models with unstructured meshes. The average convergence for the structured meshes occurred at approximately 8000 iterations and 11200 iterations for unstructured meshes. For larger models, the times saved through convergence might outweigh the time lost through generating a structured mesh. As was with the pressure drop models, the numerical uncertainty was also less for the models with structured meshes. This can be seen in Table 16. The uncertainty can be up to 4 times smaller for the structured mesh.

Table 16. Nusselt number GCI uncertainty comparison of structured and unstructured mesh for the cubic unit cells

Sample	Unstructured GCI (%)	Structured GCI (%)
Cubic20	3.42	1.35
Cubic40	4.23	1.01
Cubic60	4.09	1.60

According to the cubic unit cell heat transfer results, it is recommended to model heat transfer with unit cell lattices with structured meshes. The 9% difference in Nusselt number should be investigated in much more detail against trusted experimental data. The uncertainty for structured meshes is much smaller, but the overall accuracy remains unknown at this point. The meshing approach obviously has an impact on the accuracy, but so would the turbulence model selected. A full understanding of this model form uncertainty can only be achieved through full validation efforts.

4.2.2 Star CCM+ vs ANSYS Fluent

Just as with the pressure drop models, the cubic single unit cells with fine

structured meshes were simulated in ANSYS Fluent with the same boundary and inlet

conditions as the models in Star CCM+. The flow physics models were the same for

both cases. Figure 34 shows the Nusselt number of the single cubic unit cells for both

CFD packages. ANSYS Fluent produced a slightly higher Nusselt number for the cubic

unit cell models. The greatest change was for the Cubic60 unit cell model at 5.83 m/s,

which was only 0.81%. It is expected that the two CFD codes result in identical Nusselt

numbers as long as all the same parameters and physics models are identical. An

explanation as to the possible slight difference in results, please see the penultimate
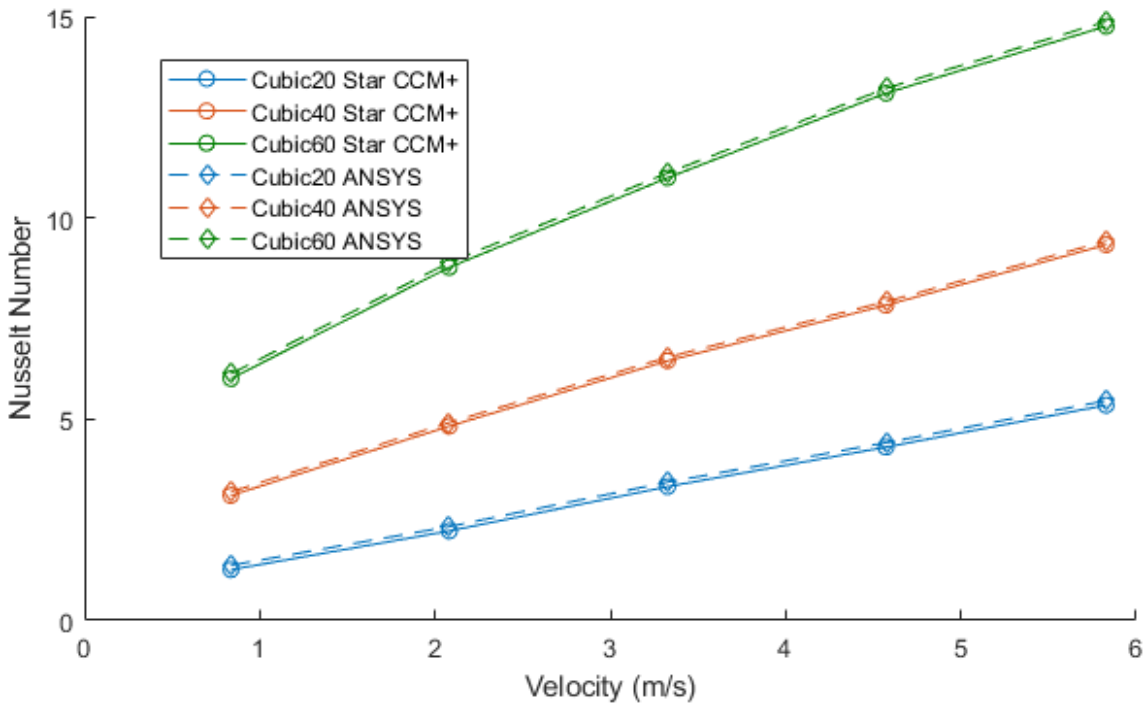
paragraph in Section 3.2.2.

Figure 34. ANSYS Fluent vs. Star CCM+ cubic unit cell Nusselt numbers using fine structured mesh.

CHAPTER 5

CONCLUSIONS

Seven samples comprised of 8 x 8 x 8 aluminum unit cells were additively manufactured in order to determine thermal hydraulic performance based on three criteria: 1) unit cell relative density, 2) unit cell geometry, and 3) unit cell orientation. Although the experimental data is currently being analyzed, this was accomplished numerically (CFD). Pressure drop and Nusselt number correlations were formed as a function of Reynolds number. These correlations, along with previously formed structural integrity correlations, will be later used to optimize the lattice for both the thermal and mechanical loads present.

According to unit cell relative density, pressure drop increased as a function of relative density. The pressure drop increased by a factor of 4.2 from the Cubic20 to Cubic40 samples and by a factor of 5.2 from the Cubic40 to Cubic60 samples. A reciprocated performance trend followed for the heat transfer results. Although the Cubic60 sample had the highest pressure drop, it was able to transfer the most heat. Nusselt number was proportional to relative density.

The four different unit cell geometries were a cubic, midpoint, octet, and diagonal unit cell. The pressure drop performance from lowest to highest was the following: Cubic40, Diagonal40, Midpoint40, and Octet40. It was concluded that amount of free path the fluid travels, the less the pressure drop. As for heat transfer performance, The Diagonal40 had the highest Nusselt number, followed by the Octet40,

Cubic40, and Midpoint40. Unlike the opposite pressure drop and heat transfer

performances according to unit cell relative density, unit cell geometry was not an exact

opposite. Finally, unit cell orientation did not prove to contribute to a difference in

pressure drop. However, the Cubic45deg transferred slightly more heat than the

Cubic40.

A study on structured and unstructered meshes were conducted on the cubic unit

cells to analyze accuracy and mesh generation time. Creating a good structured mesh can

be significantly longer than creating an automatic unstructured mesh, but the results may

need to be accurate and precise. The greatest change in pressure drop between the

unstructured and structured models was 2.2%. The greatest change in Nusselt number

was 9%.

Finally, a study was conducted to compare the pressure drop and heat transfer

data that was modeled and simulated in Star CCM+ to ANSYS Fluent. The same

boundary and inlet conditions, physics models, and all other inputs were identical. The

pressure drop differed by 0.19% and the Nusselt number differed by 0.81%. Although it

was expected to result in identical pressure drops and Nusselt numbers, the wall

functions were slightly different in each CFD program. Due to the small change in

results, the wall model difference was not further investigation.

5.1 Recommendations

Several recommendations were made based on the results and other observations.

Table 17 ranks the samples according to pressure drop and thermal performance. The top

ranking (1) signifies a low pressure drop and high Nusselt number. The Cubic20 resulted in the lowest pressure drop but also the lowest Nusselt number. The Cubic60 resulted in the complete opposite.

Table 17. Pressure drop and thermal performance rankings.

Rank	Pressure Drop	Thermal
1	Cubic20	Cubic60
2	Cubic40	Diagonal40
3	Cubic45deg	Octet40
4	Diagonal40	Cubic45deg
5	Midpoint40	Cubic40
6	Octet40	Midpoint40
7	Cubic60	Cubic20

The selection of unit cell geometry, relative density, and orientation in lattice design depends on the system's operating conditions. If the system is isothermal, then the Cubic20 unit cell is recommended. If pressure drop is not a huge concern, then the Cubic60 unit cell is recommended. If both pressure drop and heat transfer are equally important, it is recommended to design a lattice using the Diagonal40 unit cell. The diagonal unit cell has a high Nusselt number and a medium pressure drop compared to the other samples. If either pressure drop or heat transfer is more important to a system, then the correlations developed can be used to select a unit cell and relative density.

Although altering the orientation of the Cubic40 to Cubic45deg proved to transfer more heat without any noticeable change in pressure drop, this may not be the case for the other unit cell geometries. More testing would have to be done with orienting unit cells to make that conclusion.

It is recommended to use unstructured mesh for all models relating to pressure drop. The difference in pressure drop between the two meshing strategies was less than 2.5%. Some unit cells can have complex geometries and would pose a signicant challenge to develop a structured mesh. When it comes to modeling heat transfer, it is recommended to create a structured mesh for the models. The difference in Nusselt number between the two meshing types reached 9%. This difference, along with numerical uncertainty (GCI) can result in errors up to 14% when added together. Although complex geometries can require a large amount of time based on lattice size, far more accurate results will be obtained.

When it comes to selecting a CFD softare, both packages tested yielding nearly identical results keeping all parameters constant as was able. Therefore, we recommend using the one that the user has more experience with. Both Star CCM+ and ANSYS Fluent are capable of capturing the flow physics and heat transfer through complex geometries.

5.2 Future Work

As stated previously, more samples with oriented unit cell geometries need to be manufactured and tested in order to conclude that orientation improves heat transfer performance without losing additional pressure. Future work should also include an analysis on sample height. Higher levels may have a negligible effect at certain densities. Flow temperature measurements at different heights allude to this. An analysis on variable densities would also be beneficial to explore.

For CFD simulations, it would be beneficial to have a structured mesh for each of the unit cell geometries at different relative densities. Having a more variety of samples would further establish concrete results based on unit cell relative density while providing more accurate results. Up until now, only RANS models have been simulated. Future work should include exploring Large Eddy Simulations (LES), which are based on filtering rather than averaging. LES models explicitly involve the step size of the computational grid. It also makes use of fewer assumptions compared to RANS models. An example of an LES simulation comes from Salkhordeh, et al. [21]. LES models were created of a scaled High Temperature Gas Reactor (HTGR) lower plenum for assessment of tubulent mixing. Although LES computational time is longer than RANS, the error is expected to decrease since more of the flow physics is being captured.

REFERENCES

1. Meinzer, O. E., The history and development of ground-water hydrology, *Jour. Washington Acad. Sci.,* vol 24, pp. 6-32, 1934

2. Van Oijen, H., and Hoogendoorn, C. J., 1981, "Experimental Pressure Profiles Along the Vapor Channel of a Flat-Plate Heat Pipe," *Advances in Heat Pipe Technology*, Pergamon Press, Oxford, pp. 121-129

3. Mahjoob, S., and Vafai. K., 2008, "A Synthesis of Fluid and Thermal Transport Model for Metal Foam Heat Exchangers," *Int. J. Heat Mass* Transfer, 51, pp. 3701-3711

4. C.Y. Zhao "Review on thermal transport in high porosity cellular metal foams with open cells," Int. J. Heat Mass Transfer, 55 (2012), pp. 3618-3632

5. Boomsma K, Poulikakos D, Zwick F. Metal foams as compact high performance heat exchangers. Mech Mater 2003; 35:1161–76.

6. Hsieh, W. H., Wu, J. Y., Shih, W. H., and Chiu, W. C., 2004, "Experimental Investigation of Heat-Transfer Characteristics of Aluminum-Foam Heat Sinks," Int. J. Heat Mass Transfer, 47 , pp. 5149–5157

7. Tien, C. L. and Vafai, K., "Numerical study of the combined free-forced convective boundary layer flow through a highly permeable porous medium," Adv. Appl. Mech., 1990, 27, 225.

8. Calmidi, V. V., and Mahajan, R. L., 1999, ''The Effective Thermal Conductivity of High Porosity Fibrous Metal Foams,'' ASME J. Heat Transfer, 121, pp. 466–471.

9. Lee, Y. C., Zhang, W., Xie, H., and Mahajan, R. L., "Cooling of a FCHIP Package with 100 w, 1 cm2 chip," Proceedings of the 1993 ASME International Electronic Packaging Conference, Vol. 1, American Society of Mechanical Engineers, New York, 1993, pp. 419–423

10. Hsieh et al, Experimental investigation of heat-transfer characteristics of aluminium foam heat sinks, International Journal of Heat and Mass Transfer 47 (2004) 5149-5157

11. M. Vesenjak, M. Borovinsek, Z. Ren, S. Irie, S. Itoh, Behavior of Metallic foam under Shock wave loading, Metals 2 (2012) 258–264.

12. M. Bai and J. N. Chung: 'Analytical and numerical prediction of heat transfer and pressure drop in open-cell metal foams', Int. J. Therm. Sci., 2011, 50, (6), 869–880

13. Mohamed OA, Masood SH, Bhowmik JL. Optimization of fused deposition modeling process parameters: a review of current research and future prospects. Adv Manuf 2015;3(1):42–53.

14. Jacobs P F. Rapid Prototyping & Manufacturing: Fundamentals of Stereolithography. Dearborn: SME publication, 1992

15. E.O. Olakanmi, R.F. Cochrane, K.W. Dalgarno, A review on selective laser sintering/ melting (SLS/SLM) of aluminium alloy powders: processing, microstructure, and properties, Prog. Mater. Sci. 74 (10) (2015) 401–477

16. Utela BR, Storti D, Anderson RL, Ganter M. A review of process development steps for new material systems in three dimensional printing (3DP). J Manufacturing Process 2008;10:96-104.

17. Lin Cheng, Pu Zhang, Emre Biyikli, Jiaxi Bai, Joshua Robbins, Albert To, (2017) "Efficient design optimization of variable-density cellular structures for additive manufacturing: theory and experimental validation", Rapid Prototyping Journal, Vol. 23 Issue: 4, pp.660-677

18. Spiegel, M., T. Redel, Y. J. Zhang, T. Struffert, J. Hornegger, R. G. Grossman, A. Doerfler, and C. Karmonik. Tetrahedral vs. polyhedral mesh size evaluation on flow velocity and wall shear stress for cerebral hemodynamic simulation. Comput. Methods Biomech. Biomed. Eng. 14(1):9–22, 2011.

19. Roache, P. "Perspective: a method for uniform reporting of grid refinement studies," *Transactions-American Society of Mechanical Engineers Journal of Fluids Engineering*, 116 (1994) p. 405

20. A. Della Torre, G. Montenegro, G.R. Tabor, M.L. Wears, CFD characterization of flow regimes inside open cell foam substrates, Int. J. Heat Fluid Flow 50 (2014) 72-82

21. Salkhordeh, S., Clifford, C., Jana, A., & Kimber, M. L. (2018). Large Eddy Simulations of scaled HTGR lower plenum for assessment of turbulent mixing. *Nuclear Engineering and Design*, *334*, 24-41.